Shear-induced textural transitions in flow-aligning liquid crystal polymers

Dana Grecov and Alejandro D. Rey*

Department of Chemical Engineering, McGill University, 3610 University Street, Montreal, Quebec, Canada H3A 2B2
(Received 16 May 2003; published 31 December 2003)

The equations of nematodynamics are formulated, solved, and used to model textural transformations in sheared thermotropic flow-aligning nematic polymers. The solutions are classified and characterized using analytical, scaling, and numerical methods. It is found that as the shear rate increases, the pathway between an oriented nonplanar state and an oriented planar state is through texture formation and coarsening. The two shear-rate dependent dimensionless numbers that control the texture formation and coarsening process are Ericksen Er and Deborah De numbers. The emergence of texture is independent of the Deborah number, and occurs at Er$=10^4$. As the shear rate increases and Er$>10^4$ the first texture that arises is a defect lattice. Further increases of the shear rate bring De close to 1, ignite the coarsening processes, and replace the defect lattice with a defect gas. The smallest texture length scale ℓ_t occurs at the defect lattice-defect gas transition. In the defect lattice regime the texture length scale decreases with increasing shear rate as $\ell_t \propto (\dot{\gamma}-a)^{-1/2}$, while in the defect gas regime it increases as $\ell_t \propto (\dot{\gamma}-b\sqrt{(\dot{\gamma}-a)}-c)^{-1}$. Finally when De$>2$, an oriented monodomain state emerges, and the texture vanishes since coarsening overpowers defect nucleation. It is found that the texture transition cascade unoriented monodomain$\Rightarrow$defect lattice$\Rightarrow$defect gas$\Rightarrow$oriented monodomain is remarkably consistent with the experimentally observed textural transitions of sheared lyotropic nematic polymers.

I. INTRODUCTION

Nematic liquid crystals (NLCs) are textured, anisotropic, viscoelastic materials [1]. Their mechanical behavior is greatly influenced by the presence of textures, or spatial distribution of defects [2,3]. Since the rheological material functions of NLCs are functions of the underlying texture, the role of shear on the nucleation and coarsening of textures needs to be better understood.

The role of shear on texture formation and texture coarsening is greatly affected on the flow properties of NLCs [1], the molecular weight (i.e., low-molar mass or polymeric), and the class of NLC (i.e., lyotropic or thermotropic [4]). Figure 1 shows a schematic of the molecular geometry, positional disorder, and uniaxial orientational order of rigid rod nematic polymers. The partial orientational order of the molecular unit axis **u** is along the average orientation given by the director **n** (**n**·**n**$=1$). The shear flow behavior and rheology of nematic liquid crystals (NLCs) depend on the sign and magnitude of the reactive parameter λ, which is the ratio of the flow aligning effect of the deformation rate and the tumbling (rotational) effect of the vorticity [4]. For rodlike NLCs it is known that $\lambda>0$ [1]. When $\lambda>1$ the material flow aligns close to the velocity gradient direction since the rotational effect of vorticity is overcome by deformation. When $0<\lambda<1$ the director does not align close to the velocity gradient direction because the rotational effect of the vorticity dominates over the aligning effect of the deformation. Materials with $\lambda>1$ display the flow-aligning mode. For thermotropic low-molecular mass nematics the only mechanism that leads to nonaligning behavior is the proximity to the smectic A phase [5]. It has been shown that for

example 8CB ($4'$-n-octyl-4-cyanobiphenyl) is a shear flow-aligning nematic at high temperatures but as the temperature approaches the nematic-smectic A transition temperature, the material loses its ability to orient with the flow and out-of-plane orientation and defect nucleation is likely to occur [5]. Hydroxy-propyl cellulose in suitable solvents is a cholesteric lyotropic liquid crystal polymer and it exhibits nonaligning behavior at low shear-rates and flow-aligning behavior at high shear rates [4]. No systematic data that show that thermotropic liquid crystals, such as Vectra [6], are nonaligning materials, has been presented. At present there appears to be a consensus that thermotropic nematic polymers are flow aligning [7].

FIG. 1. Schematic of the molecular geometry, positional disorder, and uniaxial orientational order of rigid rod nematic polymers (NPs). The partial orientational order of the molecular unit axis **u** is along the average orientation given by the director **n** (**n**·**n**$=1$).

*Corresponding author. Email address: alejandro.rey@mcgill.ca
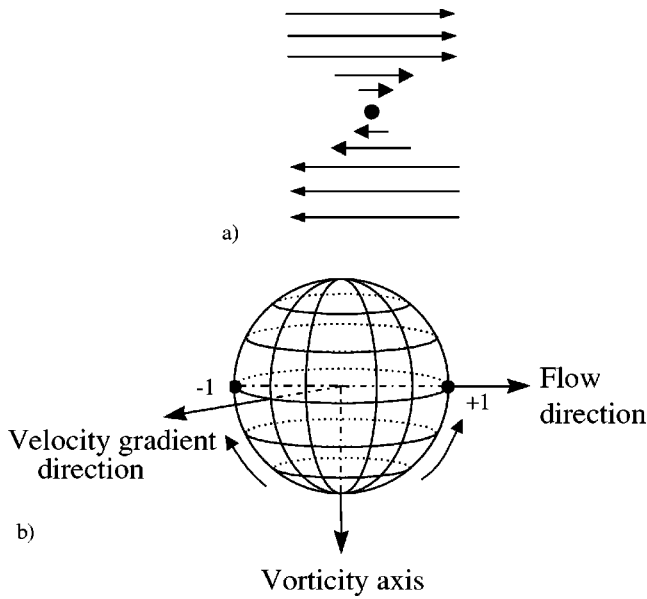
FIG. 2. (a) Schematic of a twist inversion wall in which the director rotates by π radians when traversing the wall. (b) Schematic of the unit sphere description of the director field [10] with respect to rectilinear simple shear flow. The x axis is the flow direction, the y axis the velocity gradient direction, and the z axis the vorticity axis. The equator lies in the shear (x-y) plane and the north pole and the south pole are located on the vorticity (z) axis. The director trajectory for two twist inversion walls, of charge $C = -1$, and $C = +1$, is according to the rotation sense in going from the vorticity axis to the flow direction.

Textures are spatial distributions of defects. Defects are classified according to dimensionality (D) in terms of points ($D = 0$), disclination lines ($D = 1$), and inversion walls ($D = 2$). Disclination lines can have singular or nonsingular cores [2]. The charge of a disclination line is defined by a sign ($+, -$) and a magnitude ($1/2, 1, \dots$). The sign indicates the sense of rotation when encircling the defect, and the magnitude, the amount of rotation. Inversion walls are two-dimensional nonsingular defects, in which spatially localized director gradients occur. Figure 2(a) shows an schematic of a twist inversion wall [1] in which the director rotates by π radians when traversing the wall. The continuous director rotation is localized in a thin region that defines the inversion wall thickness ξ. The surface tension of the wall is K/ξ, where K is the Frank elastic constant [8]. Inversion walls form either loops, are attached to other defects, or to the bounding surfaces. Once nucleated, inversion walls can shrink, pinch, or annihilate with other walls or other defects [9]. All these nucleation and coarsening defect processes have an impact on the viscoelastic response of the system, since elastic and dissipative mechanisms are involved. Models and theories of nucleation and coarsening of textures under flow is a topic of current interest. (see, for example, Refs. [1,9–13]). The anisotropic properties of nematics give rise to novel field-induced reorientation mechanisms and defect nucleation [8,14,15]. The emergence of field-induced inversion walls in several lyotropic and thermotropic nematic polymers has been well characterized [1,10,16–20]. Typi-

cally inversion walls in NLCs under external fields arise because two equivalent reorientation (rotation) mechanisms are possible. The net result is a field-aligned sample with trapped thin layers that separate regions of clockwise rotations from those of anticlockwise rotation. In many nematic polymers the inversion walls are organized into long-lived periodic structures (i.e., defect lattice) [1,16,21–23]. Inversion walls are classified according to the elastic (i.e., splay, bend, and twist) modes of deformation [8]. In this paper we restrict the discussion to twist inversion walls [24], in which the director **n** lies in a plane parallel to the wall. Twist inversion walls are characterize by a topological charge C, given by

$$C = \frac{\Delta \psi}{\pi}, \tag{1}$$

where $\Delta \psi$ is the total director rotation while traversing the wall. As in disclination lines, the sign of the charge define the sense of rotation. Since sheared flow-aligning nematic polymers orient very close to the velocity direction, an inversion wall formation is expected if the initial orientation is orthogonal to the imposed flow. In addition, if the flow-aligning angle is sufficiently small, say less than several degrees, the walls are essentially twist walls. Figure 2(b) is a schematic of the unit sphere description of the director field [25], where the x axis is the flow direction, the y axis the velocity gradient direction, and the z axis (out of the plane of the paper) the vorticity axis. The equator lies in the shear (x-y) plane and the north pole and the south pole are located on the vorticity (z) axis. The figure shows the director trajectory for two twist inversion walls, of charges $C = -1$ and $+1$, according to the rotation sense in going from the vorticity axis to the flow. In this paper we use shear-induced generation of twist inversion walls as a model for texture generation.

As mentioned above, each class of liquid crystals displays a distinguishing number of textures. Textures exist in small-molecule nematics, both flow aligning and tumbling [26–28], but are much more persistent in LCPs, due to the high viscosities of the latter [4]. As mentioned above, in both thermotropic and lyotropic liquid crystal polymers (LCPs), it is known that defects influence the microstructure and rheology [29]. The connection between textures and rheology of lyotropic LCP has been experimentally characterized [30–34]. For thermotropic LCPs less progress has been made, as a consequence of experimental difficulties [7]. However, there are studies of the textural transitions in thermotropic LCPs (TLCPs) [29,35–37].

The theoretical and computational framework for the widely reported flow-induced texture and pattern formation phenomena in liquid crystal materials has been investigated in several studies [1]. For low-molecular weight liquid crystals [38–40], it is found that for low shear rates the flow may become unstable when the director is perpendicular to the shear plane. Furthermore, in Ref. [41] this study is extended to the shearing flow of tumbling LCPs. Moreover, a texture involving twist distortions has been predicted in a nonlinear fast flow of a flow-aligning nematic [42]. Thus the condition

$\lambda > 1$ is not guaranteed that a uniform molecular alignment will emerge, as previously believed.

Numerical integration of the classical Leslie-Ericksen nematodynamics equations [43,44] has shown that band formation during the start-up of sheared LCPs can be explained by twist distortions which dominate in flow over splay and bend. A very complete analysis of the symmetry-breaking transient states with the director out of the shear plane, which partially coexist with the in-plane states, is given in Ref. [45] for rodlike molecular weight and polymeric LCs in simple shear flow, using a nonlinear relaxation equation for the alignment tensor. The hydrodynamics induced symmetries and broken symmetries for uniaxial nematic liquid crystals are presented in Ref. [46]. A computational simulation, using a tensorial theory, is used in Ref. [47] to study the spatial inhomogeny of the director field, which plays an important role in a highly textured thermotropic LCP. The flow in lyotropic LCPs has been investigated through numerical simulations, in several studies, using Landau–de Gennes theory [11], Doi-Marruci-Greco theory [48], and extensions of Doi theory for nematic polymers [49]. They all capture important aspects of flow-induced pattern formation. The aim of this paper is to extend the study of flow-induced texture generation to flow-aligning thermotropic polymeric NLCs.

The specific objectives of this paper are (1) to elucidate the mechanisms that control textural transformation in sheared, flow-aligning, rigid-rod, nematic polymers, under isothermal conditions; (2) to characterize how the texture length scale depends on the imposed shear rate; and (3) to explain the observed [31,32] shear-induced texture cascade unoriented monodomain⇒defect texture⇒oriented monodomain using the classical equation of nemato-dyanmics in conjunction with analytical, scaling, and computational methods.

This paper is organized as follows. In Sec. II we present the governing equations that describe the microstructure for polymeric liquid crystals under arbitrary flow, and the numerical procedure. Analytical results are presented in Sec. III. In Sec. IV we present, classify, and discuss the simulation results. Section V discusses the essence of the predicted results in conjunction with relevant experimental results. Section VI presents the conclusions.

II. THEORY AND GOVERNING EQUATIONS

In this section, we present the Landau–de Gennes theory for nematic liquid crystals, and the parametric equations used to describe liquid crystalline polymers texture formation. As mentioned above, the theory is well suited to simulate texture formation since defects are nonsingular solutions to the governing equations. In this paper we study a rectilinear simple start-up shear flow with Cartesian coordinates, as shown in Fig. 3(a). The lower plate is fixed and the upper plate starts moving at $t=0$ with a known constant velocity V; the plate separation is H. The z axis is coaxial with the vorticity axis and the shear plane is spanned by the x-y axes.

A. Landau–de Gennes mesoscopic model for liquid crystal polymers

The microstructure of liquid crystal polymers (LCPs) is described conveniently in terms of a second order, symmetric and traceless tensor order parameter $\mathbf{Q}$ [8]:
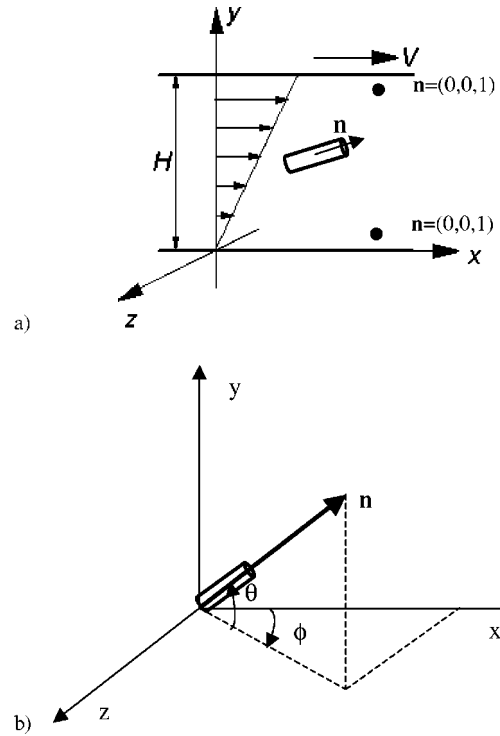
FIG. 3. Definition of the flow geometry and coordinates system for simple shear flow. (a) The lower plate is at rest and the upper plate moves in the x direction with a constant velocity V, H is the gap separation. (b) Cartesian coordinate system with x the flow direction, y the velocity gradient direction, and z the vorticity axis. The director $\mathbf{n}$ is defined by the tilt angle θ and the twist angle ϕ.

$$\mathbf{Q} = \int \left(\mathbf{u}\mathbf{u} - \frac{\mathbf{I}}{3} \right) \omega d^2\mathbf{u}, \qquad (2)$$

where $\mathbf{u}$ is the unit vector parallel to the rodlike molecules (see Fig. 1), $\mathbf{I}$ is unit tensor, and ω is the orientation distribution function. The symmetric and traceless tensor order parameter $\mathbf{Q}$ can be expressed by

$$\mathbf{Q} = S\left(\mathbf{n}\mathbf{n} - \frac{1}{3}\mathbf{I} \right) + \frac{1}{3}P(\mathbf{m}\mathbf{m} - \mathbf{l}\mathbf{l}), \qquad (3)$$

where the following restrictions apply:

$$\mathbf{Q} = \mathbf{Q}^T, \quad \mathrm{tr}(\mathbf{Q}) = 0, \quad -\frac{1}{2} \leq S \leq 1, \quad -\frac{3}{2} \leq P \leq \frac{3}{2}, \quad (4)$$

$$\mathbf{n}\cdot\mathbf{n} = \mathbf{m}\cdot\mathbf{m} = \mathbf{l}\cdot\mathbf{l} = 1, \quad \mathbf{n}\mathbf{n} + \mathbf{m}\mathbf{m} + \mathbf{l}\mathbf{l} = \mathbf{I} = \begin{bmatrix} 1 & 0 & 0 \\ 0 & 1 & 0 \\ 0 & 0 & 1 \end{bmatrix}. \qquad (5)$$

The uniaxial director $\mathbf{n}$ corresponds to the maximum eigenvalue $\mathsf{s}_n = 2/3S$, the biaxial director $\mathbf{m}$ corresponds the second largest eigenvalue $\mathsf{s}_m = -1/3(S-P)$, and the second biaxial director $\mathbf{l}$ ($=\mathbf{n}\times\mathbf{m}$) corresponds to the smallest eigenvalue $\mathsf{s}_\ell = -1/3(S+P)$. The orientation is defined completely by the orthogonal director triad ($\mathbf{n}$, $\mathbf{m}$, $\mathbf{l}$). The mag-

nitude of the uniaxial scalar order parameter S is a measure of the molecular alignment along the uniaxial director $\mathbf{n}$, and is given as $S = 3/2\,(\mathbf{n} \cdot \mathbf{Q} \cdot \mathbf{n})$. The magnitude of the biaxial scalar order parameter P is a measure of the molecular alignment in a plan perpendicular to the direction of uniaxial director $\mathbf{n}$, and is given by $P = 3/2(\mathbf{m} \cdot \mathbf{Q} \cdot \mathbf{m} - \mathbf{l} \cdot \mathbf{Q} \cdot \mathbf{l})$.

The Landau–de Gennes theory of liquid crystals [50] describes the viscoelastic behavior of nematic liquid crystals using the second moment of the orientation distribution function, known as the tensor order parameter $\mathbf{Q}$. The governing equations for liquid crystal flows follow from the dissipation function Δ:

$$\Delta = \mathbf{t}^s : \mathbf{A} + \mu kT \Theta \cdot \hat{\mathbf{Q}}, \tag{7}$$

where $\mathbf{t}^s$ is the viscoelastic stress tensor, μ is the concentration of molecules per unit volume, k the Boltzmann constant, and T the absolute temperature, $\mathbf{A}$ is the symmetric traceless rate of deformation tensor, Θ is the molecular field, and $\hat{\mathbf{Q}}$ is the Jaumann derivative of the tensor order parameter, given by

$$\hat{\mathbf{Q}} = \frac{\partial \mathbf{Q}}{\partial t} + (\mathbf{v} \cdot \nabla)\mathbf{Q} - \mathbf{W} \cdot \mathbf{Q} + \mathbf{Q} \cdot \mathbf{W}, \tag{8a}$$

$$\mathbf{W} = \frac{1}{2}(\nabla \mathbf{v} - \nabla \mathbf{v}^T), \tag{8b}$$

$$\mathbf{A} = \frac{1}{2}(\nabla \mathbf{v} + \nabla \mathbf{v}^T), \tag{8c}$$

$$(\mu kT)\Theta = -\left[\frac{\delta F}{\delta \mathbf{Q}}\right]^{[s]} = \left[\frac{\partial f}{\partial \mathbf{Q}} - \nabla \cdot \frac{\partial f}{\partial \nabla \mathbf{Q}}\right]^{[s]}, \tag{8d}$$

where F is the total free energy and f is the free energy density:

$$f = f_{\mathrm{sr}} + f_{\mathrm{lr}}, \tag{9a}$$

$$f_{\mathrm{sr}} = (\mu kT)\left[\frac{1}{2}\left(1 - \frac{1}{3}U\right)\mathbf{Q} : \mathbf{Q} - \frac{1}{3}U\mathbf{Q} : (\mathbf{Q} \cdot \mathbf{Q})\right.$$
$$\left. + \frac{1}{4}U(\mathbf{Q} : \mathbf{Q})^2, \right] \tag{9b}$$

$$f_{\mathrm{lr}} = \frac{L_1}{2\mu kT}\left[\{\nabla \mathbf{Q} : (\nabla \mathbf{Q})^T\} + \frac{L_2}{2ckT}(\nabla \cdot \mathbf{Q}) \cdot (\nabla \cdot \mathbf{Q})\right], \tag{9c}$$

where f_{sr} is the homogeneous (short range) energy density, f_{lr} is the gradient (long range) energy density, $U = 3T^*/T$ is the nematic potential, T^* is the isotropic-nematic transition temperature, L_1 and L_2 are the Landau coefficients, and the superscript $[s]$ denotes symmetric and traceless. Using the Landau–de Gennes free energy density, the molecular field is given by

$$-\left[\frac{\delta F}{\delta \mathbf{Q}}\right]^{[s]} = (\mu kT)\Theta = -(\mu kT)\left[\left(1 - \frac{1}{3}U\right)\mathbf{Q} - U\mathbf{Q} \cdot \mathbf{Q}\right.$$
$$\left. + U\left\{(\mathbf{Q} : \mathbf{Q})\mathbf{Q} + \frac{1}{3}(\mathbf{Q} : \mathbf{Q})\mathbf{I}\right\}\right] + (\mu kT)$$
$$\times \left[\frac{L_1}{\mu kT}\nabla^2 \mathbf{Q} + \frac{1}{2}\frac{L_2}{\mu kT}\left(\nabla(\nabla \cdot \mathbf{Q})\right.\right.$$
$$\left.\left. + \{\nabla(\nabla \cdot \mathbf{Q})\}^T - \frac{2}{3}\mathrm{tr}\{\nabla(\nabla \cdot \mathbf{Q})\}\mathbf{I}\right)\right], \tag{10}$$

and contains short-range (homogeneous) and long-range (gradient) contributions. Expanding the forces ($\mathbf{t}^s$, $\hat{\mathbf{Q}}$) in terms of fluxes ($\mathbf{A}$, $\mu kT\Theta$), and taking into account thermodynamic restrictions and the symmetry and tracelessness of the forces and fluxes we can obtain the equations for $\mathbf{t}^s$ and $\hat{\mathbf{Q}}$. In this paper we concentrate on the dynamics of $\mathbf{Q}$, and hence we assume that the velocity field of the shear flow is known and given by

$$\mathbf{V} = (\dot{\gamma}y, 0, 0), \tag{11}$$

where the constant shear rate is given by $\dot{\gamma} = V/H$. The dynamics of the tensor order parameter is given by the following sum of flow $\mathbb{F}$, short-range Θ^{sr}, and long-range Θ^{lr} contributions [51]:

$$\hat{\mathbf{Q}} = \mathbb{F}(\mathbf{Q}, \nabla \mathbf{v}) + \Theta, \tag{12a}$$

$$\Theta = \Theta^{\mathrm{sr}}(\mathbf{Q}, \bar{D}_r(\mathbf{Q})) + \Theta^{\mathrm{lr}}(\nabla \mathbf{Q}), \tag{12b}$$

(i) flow contribution $\mathbb{F}$,

$$\mathbb{F}(\mathbf{Q}, \nabla \mathbf{v}) = \frac{2}{3}\beta \mathbf{A} + \beta\left[\mathbf{A} \cdot \mathbf{Q} + \mathbf{Q} \cdot \mathbf{A} - \frac{2}{3}(\mathbf{A} : \mathbf{Q})\mathbf{I}\right]$$
$$-\frac{1}{2}\beta[(\mathbf{A} : \mathbf{Q})\mathbf{Q} + \mathbf{A} \cdot \mathbf{Q} \cdot \mathbf{Q} + \mathbf{Q} \cdot \mathbf{A} \cdot \mathbf{Q} + \mathbf{Q} \cdot \mathbf{Q} \cdot \mathbf{A}$$
$$-\{(\mathbf{Q} \cdot \mathbf{Q}) : \mathbf{A}\}\mathbf{I}], \tag{13}$$

(ii) short-range elastic contribution Θ^{sr},

$$\Theta^{\mathrm{sr}}(\mathbf{Q}, \bar{D}_r(\mathbf{Q})) = -6\bar{D}_r\left[\left(1 - \frac{1}{3}U\right)\mathbf{Q} - U\mathbf{Q} \cdot \mathbf{Q}\right.$$
$$\left. + U\left\{(\mathbf{Q} : \mathbf{Q})\mathbf{Q} + \frac{1}{3}(\mathbf{Q} : \mathbf{Q})\mathbf{I}\right\}\right], \tag{14}$$

and (iii) long-range elastic contribution Θ^{lr},

$$\Theta^{\mathrm{lr}}(\nabla \cdot \mathbf{Q}) = 6\bar{D}_r\left[\frac{L_1}{\mu kT}\nabla^2 \mathbf{Q} + \frac{1}{2}\frac{L_2}{\mu kT}\left(\nabla(\nabla \cdot \mathbf{Q})\right.\right.$$
$$\left.\left. + \{\nabla(\nabla \cdot \mathbf{Q})\}^T - \frac{2}{3}\mathrm{tr}\{\nabla(\nabla \cdot \mathbf{Q})\}\mathbf{I}\right)\right], \tag{15}$$

$$\bar{D}_r = \frac{D_r}{\left(1 - \frac{3}{2}\mathbf{Q}:\mathbf{Q}\right)^2}, \tag{16}$$

where $\bar{D}_r$ is the microstructure dependent rotational diffusivity, D_r is the pre-averaged rotational diffusivity here taken to be constant and β is a thermodynamic parameter which is not determined by molecular shape since our model contains no specific molecular information. The dimensionless form of the governing equation for the tensor order parameter $\mathbf{Q}$ is

$$
\begin{aligned}
\mathrm{Er}\hat{\mathbf{Q}}^* = \mathrm{Er}&\left[\frac{2}{3}\beta\mathbf{A}^* + \beta\left[\mathbf{A}^*\cdot\mathbf{Q} + \mathbf{Q}\cdot\mathbf{A}^* - \frac{2}{3}(\mathbf{A}^*:\mathbf{Q})\mathbf{I}\right]\right.\\
&- \frac{1}{2}\beta[(\mathbf{A}^*:\mathbf{Q})\mathbf{Q} + \mathbf{A}^*\cdot\mathbf{Q}\cdot\mathbf{Q} + \mathbf{Q}\cdot\mathbf{A}^*\cdot\mathbf{Q} + \mathbf{Q}\cdot\mathbf{Q}\cdot\mathbf{A}^*\\
&- \{(\mathbf{Q}\cdot\mathbf{Q}):\mathbf{A}^*\}\mathbf{I}]\bigg] - \frac{3}{U}\cdot\frac{R}{\left(1 - \frac{3}{2}\mathbf{Q}:\mathbf{Q}\right)^2}\\
&\times\left[\left(1 - \frac{1}{3}U\right)\mathbf{Q} - U\mathbf{Q}\cdot\mathbf{Q} + U\left\{(\mathbf{Q}:\mathbf{Q})\mathbf{Q}\right.\right.\\
&+ \frac{1}{3}(\mathbf{Q}:\mathbf{Q})\mathbf{I}\bigg\}\bigg] + \frac{3}{\left(1 - \frac{3}{2}\mathbf{Q}:\mathbf{Q}\right)^2}\left[\boldsymbol{\nabla}^{*2}\mathbf{Q}\right.\\
&+ \frac{1}{2}L_2^*\left(\boldsymbol{\nabla}^*(\boldsymbol{\nabla}^*\cdot\mathbf{Q}) + \{\boldsymbol{\nabla}^*(\boldsymbol{\nabla}^*\cdot\mathbf{Q})\}^T\right.\\
&- \frac{2}{3}\mathrm{tr}\{\boldsymbol{\nabla}^*(\boldsymbol{\nabla}^*\cdot\mathbf{Q})\}\mathbf{I}\bigg)\bigg],
\end{aligned}
\tag{17}
$$

$$t^* = \dot{\gamma}t = \gamma, \quad \mathbf{A}^* = \frac{\mathbf{A}}{\dot{\gamma}}, \quad \mathbf{W}^* = \frac{\mathbf{W}}{\dot{\gamma}},$$

$$\boldsymbol{\nabla}^* = H\boldsymbol{\nabla}, \quad L_2^* = \frac{L_2}{L_1}, \tag{18}$$

where the star superscript denotes dimensionless quantities, $\dot{\gamma}$ is the shear rate, and γ is the strain. The dimensionless free energy density f^* is given by

$$f^* = \frac{3}{U}f_{\mathrm{sr}}^* + \frac{3}{R}f_{\mathrm{lr}}^*. \tag{19}$$

The dimensionless numbers Er (Ericksen number) and energy ratio R [50] are given by

$$\mathrm{Er} = \frac{\dot{\gamma}H^2\eta}{L_1}, \tag{20a}$$

$$R = \frac{3H^2\mu k T^*}{L_1}, \tag{20b}$$

$$\eta = \frac{\mu k T^*}{2D_r}, \tag{20c}$$

and are the ratio of viscous flow effects to long-range order elasticity, and short-range order elasticity to long-range order elasticity, respectively. Here η is a characteristic viscosity. The Deborah number De, or the ratio between flow effect and short range energy effect, is given by

$$\mathrm{De} = \frac{\mathrm{Er}}{R} = \frac{\dot{\gamma}}{6D_r}, \tag{21}$$

and its magnitude controls the amplitude of effects associated with the scalar order parameters.

The Landau–de Gennes model for nematic liquid crystals has an external length scale l_e and an internal length scale l_i as follows:

$$\ell_e = H, \quad \ell_i = \sqrt{\frac{L_1}{3\mu k T^*}}, \quad \ell_e \gg \ell_i. \tag{22}$$

It should be noted that the external length scale governs the directors' orientation ($\mathbf{n}, \mathbf{m}, \mathbf{l}$) while the internal length scale governs the scalar order parameter (S, P). The external τ_e and internal τ_i time scales of model are ordered as follows:

$$\tau_e = \frac{\eta H^2}{3L_1}, \quad \tau_i = \frac{1}{D_r}, \quad \tau_e \gg \tau_i. \tag{23}$$

The external time scale describes slow orientation variations and the internal length scale describes fast order parameter variations. Finally the presence of shear flow of rate $\dot{\gamma}$ introduces a flow time scale τ_f:

$$\tau_f = \frac{1}{\dot{\gamma}}, \tag{24}$$

and a flow length scale ℓ_f:

$$\ell_f = \sqrt{\frac{\delta}{\dot{\gamma}}}, \quad \delta = \frac{L_1}{\eta}, \tag{25}$$

where δ is the orientation diffusivity. The relation between the time scales, length scales and the dimensionless numbers are

$$\mathrm{Er} = \frac{\tau_e}{\tau_f} = \frac{H^2}{\ell_f^2}, \tag{26a}$$

$$R = \frac{\tau_e}{\tau_i} = \frac{H^2}{\ell_i^2}, \tag{26b}$$

$$\mathrm{De} = \frac{\tau_i}{\tau_f} = \frac{\ell_i^2}{\ell_f^2}. \tag{26c}$$

Related to the values of Deborah numbers we have two processes. (a) Orientation process (De$\ll$1): the time scale ordering is $\tau_i < \tau_f < \tau_e$, the orientation processes dominate the rheology, and the scalar order parameter is close to its equilibrium value. In this regime the flow affects the eigenvectors of $\mathbf{Q}$, but does not affect the eigenvalues of $\mathbf{Q}$. (b) Molecular

process (De>1): the time scales ordering is $\tau_f < \tau_i < \tau_e$, and the flow affects the eigenvectors and eigenvalues of **Q**.

B. Computational methods and auxiliary data

The model equations (17) are a set of five coupled non-linear parabolic partial differential equations. The equations are solved using Galerkin finite elements for spatial discretization and a fourth order Runge-Kutta time adaptive method. Convergence and mesh independence were established in all cases using standard methods. Spatial discretization was judiciously selected taking into account the length scale of our model. The selected adaptive time integration scheme is able to efficiently take into account the stiffness that rises due to the disparity between time scale: $\tau_i \ll \tau_e$.

The boundary conditions for **Q** are

$$\mathbf{Q}_s(y^*=0)=\mathbf{Q}_s(y^*=1)=S_{eq}\left(\mathbf{n}_s\mathbf{n}_s-\frac{\mathbf{I}}{3}\right), \quad (27a)$$

$$\mathbf{n}_s=(0,0,1), \quad (27b)$$

$$S_{eq}=\frac{1}{4}+\frac{3}{4}\sqrt{1-\frac{8}{3U}}, \quad (27c)$$

describing a fixed director orientation along the vorticity axis, a uniaxial state with the scalar order parameter equal to its equilibrium value. The initial state is assumed to be uniaxial and at equilibrium. The orientation of the director at $t=0$ is assumed to be parallel to $\mathbf{n}_s$, with thermal fluctuations introduced by infinitesimal Gaussian noise. The thermodynamic parameter β and the nematic potential are used to calculate the reactive parameter λ, which indicates if the system is flow aligning or not. In this paper the values for these parameters are chosen to assure that $\lambda < 1$ (flow-aligning system): $U=4$, $\beta=1.2$. The selected ranges for the dimensionless parameters are $10^3 < R < 10^6$, $0 < \mathrm{Er} < 2 \times 10^7$, and $0 < \mathrm{De} < 20$.

III. ANALYTICAL RESULTS

A. Orientation modes predicted by the Leslie-Ericksen model

The most successful and established theory applicable to slow uniaxial nematic flows is that of Leslie and Ericksen [52]. It was shown [50] that when the ratio between the Ericksen number and R is insignificant (i.e., slow flow), the Landau–de Gennes model reduces to the Leslie-Ericksen (LE) theory, when the splay and bend elastic modulus [see Eqs. (28)] are equal. Since the Landau–de Gennes model at sufficiently slow flows becomes the LE model, it is useful to use the easily obtained predictions of the LE model in order to explain and classify the response of the more complicated Landau–de Gennes model. We note that all our computational results discussed in the following sections were obtained using the original Landau–de Gennes equations (17).

As mentioned above the LE theory neglects the short-range order elasticity, and hence it is unable to describe the changes of the scalar order parameter due to the imposition of sufficiently strong flow. Consequently, in this theory, the microstructure is described by the director **n** and the scalar order parameter S is assumed to remain constant, that is, unaffected by the flow, and always equal to its value at equilibrium: $S=S_{eq}$, while the biaxial order parameter P is equal to zero. The total extra-stress tensor $\mathbf{t}^t$ and the director balance equation in the LE theory [52] are

$$\mathbf{t}^t=p\,\delta-\frac{\partial f_n}{(\partial\nabla\mathbf{n})^T}\cdot\nabla\mathbf{n}+\alpha_1\mathbf{A:nnnn}+\alpha_2\mathbf{nM}+\alpha_3\mathbf{Mn}+\alpha_4\mathbf{A}$$

$$+\alpha_5\mathbf{nn}\cdot\mathbf{A}+\alpha_6\mathbf{A}\cdot\mathbf{nn}, \quad (28a)$$

$$0=\mathbf{\Gamma}^e+\mathbf{\Gamma}^v, \quad (28b)$$

$$\mathbf{\Gamma}^e=-\mathbf{n}\times\left(\frac{\partial f_n}{\partial\mathbf{n}}-\nabla\cdot\frac{\partial f_n}{(\partial\nabla\mathbf{n})}\right),$$

$$\mathbf{\Gamma}^v=-\mathbf{n}\times(\gamma_1\mathbf{M}+\gamma_2\mathbf{A}\cdot\mathbf{n}), \quad (29a)$$

$$\gamma_1=\alpha_3-\alpha_2, \quad \gamma_2=\alpha_6-\alpha_5 \quad (29b)$$

where f_n is the Frank long-range energy density, given in terms of the following splay (K_{11}), twist (K_{22}), and bend (K_{33}) modes:

$$2f_n=K_{11}(\nabla\cdot\mathbf{n})^2+K_{22}(\mathbf{n}\cdot\nabla\times\mathbf{n})^2+K_{33}|\mathbf{n}m\times\nabla\times\mathbf{n}|^2. \quad (30)$$

A is the rate of deformation tensor, **M** is the Jaumann derivative of the director **n**:

$$\mathbf{M}=\dot{\mathbf{n}}-\mathbf{n}\cdot\mathbf{W}. \quad (31)$$

$\{\alpha_i\}$, $i=1$ and 6, are the six Leslie viscosities coefficients, where only five of these are independent due to Parodi's relation [53]

$$\alpha_6-\alpha_5=\alpha_2+\alpha_3. \quad (32)$$

In the Landau–de Gennes model used here [Eq. (17)] $K_{11}=K_{33}$. To break the splay-bend equality higher order terms are required, but for the present paper they are unnecessary because the phenomena of interest is independent of this anisotropy. In the LE theory the reactive parameter λ that controls flow alignment is given by

$$\lambda=-\frac{\gamma_2}{\gamma_1}=-\frac{\alpha_2+\alpha_3}{\alpha_3-\alpha_2}. \quad (33)$$

As mentioned above, the characteristic flow behavior of a nematic liquid crystal depends only the sign and magnitude of the reactive parameter or equivalently on the Leslie viscosity coefficients α_2 and α_3. When shearing a nematic liquid crystal two different types of flow behavior are possible, depending on the signs of α_2 and α_3. For rodlike molecules, α_3 is always negative, while α_2 can be negative for flow alignment systems ($\lambda > 1$) or positive for nonalignment systems [54] ($0 < \lambda < 1$). The flow-alignment angle is known as the Leslie angle θ_{al}, and is given by
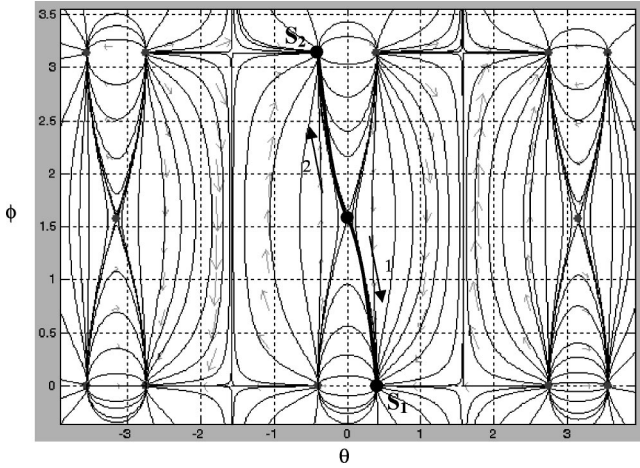
FIG. 4. Phase plane trajectories in the θ-ϕ plane for $\lambda = 1.43$. The stable (S_1) sink nodes correspond to the Leslie θ_L angle, and the stable sink node (S_2) to $-\theta_L$ while the twist angle is equal to π. The vorticity direction (z axis) is an unstable saddle point. If the director is initial aligned along the vorticity direction, ($\theta = 0, \phi = 90$) the director can take trajectory 1, to the stable sink S_1 corresponding to θ_L and $\phi = 0$ or trajectory 2, to the stable sink S_2, corresponding to the antipode $-\theta_L$ and $\phi = \pi$.

$$\cos 2\theta_{al} = \frac{1}{\lambda} \qquad (34)$$

and exists for $\lambda > 1$. As seen from Eq. (34), for shear-aligning rods the flow tends to align the average molecular orientation along the flow direction.

Next we briefly present the LE predictions to simple shear when the director is along the vorticity that are relevant to this paper. In Cartesian component form, the director is written as [Fig. 3(b)] $\mathbf{n} = (\cos\theta\cos\phi, \sin\theta, \cos\theta\sin\phi)$, where θ is the tilt angle and ϕ is the twist angle. The in-plane orientation corresponds to $\phi = 0$, and the out-of-plane orientation corresponds to $\phi \neq 0$. The velocity gradient for shear can be assumed uniform across the sample: $\mathbf{v} = (\dot{\gamma}y, 0, 0)$. Replacing the director and velocity fields in Eqs. (28) in the angular momentum balance equation (29), and neglecting the Frank elasticity, the following coupled nonlinear differential equations result [52]:

$$(\alpha_3 - \alpha_2)\frac{d\theta}{dt} + \dot{\gamma}(\alpha_3\cos^2\theta - \alpha_2\sin^2\theta)\cos\phi = 0, \qquad (35a)$$

$$(\alpha_3 - \alpha_2)\cos\theta\frac{d\phi}{dt} - \dot{\gamma}\alpha_2\sin\theta\sin\phi = 0. \qquad (35b)$$

Figure 4 shows the phase plane trajectories in the θ-ϕ plane for $\lambda = 1.43$, obtained by solving Eqs. (36). The stable (S_1) sink nodes correspond to the Leslie θ_L angle, and the stable sink node (S_2) to $-\theta_L$ while the twist angle is equal to π. The vorticity direction (z axis) is an unstable saddle point (Fig. 4). We can see that if the director is initial aligned along the vorticity direction ($\theta = 0, \phi = 90$), the director can take

trajectory 1 to the stable sink S_1 corresponding to θ_L and $\phi = 0$ or trajectory 2 to the stable sink S_2, corresponding to the antipode $-\theta_L$ and $\phi = \pi$.

Introducing elasticity allows for two new features. If Er is sufficiently low, flow is weak, and the boundary effects stabilize the orientation along the vorticity direction. If Er is sufficiently large the two equivalent flow attractors become dominant. In this case a director field aligned along the vorticity axis may evolve to a unique attractor, or to both attractors. Since evolving to both attractors introduce further distortions, these modes may arise at higher Er. In the presence of one attractor n_x is symmetric, while in the equipresence of two attractors it is antisymmetric. Multisampling of the two attractors gives rise to a layered mode. Thus the LE model that subjecting a NLC with $\mathbf{n} = (0,0,1)$ the following solution multiplicity: (a) Homogeneous mode $(H): 0 < x < H$, $\mathbf{n} = (0,0,1)$. (b) Symmetric mode $(S): 0 < x < H$, sgn$(n_x) = +$. (c) Antisymmetric mode $(AT): 0 < x < H/2$, sgn$(n_x) = +$; $H/2 < x < H$, sgn$(n_x) = -$. (d) Defect lattice mode $(DL): 0 < x < \ell$, sgn$(n_x) = +$; $\ell < x < 2\ell$, sgn$(n_x) = -, \dots$.

sgn is the sign, and ℓ is the layer thickness and where the other trivially distinct cases are omitted for brevity. For example the equivalent S mode to the one stated in (a) corresponds to sgn$(n_x) = -$, and so on. Modes (a)-(b)-(c) have been previously analyzed [55,56]. The symmetry breakings (nonhomogeneous modes) are induced by the flow. The minimum Ericksen number required for the nonhomogeneous modes (b)-(c)-(d) can be predicted using linear stability analysis. For simplicity we assume the constant approximation $(K_{11} = K_{22} = K_{33} = K)$, and neglect backflow (hydrodynamic flow induced by orientation, for details see Ref. [53]). For a cell of thickness H, under a constant shear rate $\dot{\gamma}$, no backflow, and aligned along the vorticity ($n_z = 1$) at the bounding surfaces ($y = \pm H/2$) the linear LE equations for the twist φ' and tilt θ' angles measured from the vorticity (z) axis are

$$K\frac{d^2\theta'}{dy^2} = \alpha_3\dot{\gamma}\varphi', \qquad K\frac{d^2\varphi'}{dy^2} = \alpha_2\dot{\gamma}\theta'. \qquad (36)$$

The equations admit the following multiplicity:

$$\varphi' = \varphi_0 \cos\left[\frac{n\pi z}{H} + (n-1)\frac{\pi}{2}\right],$$

$$\theta' = \theta_0 \cos\left[\frac{n\pi z}{H} + (n-1)\frac{\pi}{2}\right], \qquad n = 1, 2, \dots. \qquad (37)$$

The $n = 0$ mode represents the symmetric mode, $n = 1$ the antisymmetric mode, and $n > 2$ the defect mode. The nth mode exists when the Ericksen number satisfies

$$\text{Er} = \frac{\dot{\gamma}H^2K}{\sqrt{\alpha_2\alpha_3}} > (n\pi)^2, \qquad (38)$$

where we used a slightly different definition of the Ericksen number, to follow the classical results of Pieranski and Guyon [57]. Starting with the director along the vorticity and

with strong surface anchoring, neglecting backflow, when the Ericksen number is slightly greater than π^2, we can observe the symmetric, antisymmetric or the defect solutions under simple shear flow. Which solution is selected for a given Er is determined by the basin of attraction of each mode, as shown below.

B. Single and multiple inversion walls

The steady LE equations including elasticity, and neglecting back-flow for the tilt θ and twist ϕ angles are

$$K\frac{d^2\theta}{dy^2} = +\dot\gamma(\alpha_3\cos^2\theta - \alpha_2\sin^2\theta)\cos\phi, \quad (39a)$$

$$K\cos\theta\frac{d^2\phi}{dy^2} = -\dot\gamma\alpha_2\sin\theta\sin\phi. \quad (39b)$$

At sufficiently high shear rates $\dot\gamma$ we can assume that the tilt angle θ is aligned along the Leslie angle θ_L, and the latter equation (39b) gives the steady sine-Gordon equation:

$$\xi^2\frac{d^2\varphi}{dy^2} = \sin\varphi, \quad \xi = \sqrt{\frac{K}{\dot\gamma|\alpha_2|}}\sqrt{\frac{\lambda-1}{\lambda+1}}, \quad (40)$$

where α_2 was assumed to be negative, in accordance with flow-aligning rod-like nematics [54], where ξ is the coherence length or wall thickness. In terms of the flow thickness, introduced in Eq. (40), the wall thickness is

$$\xi = \sigma\cdot\ell_f, \quad \sigma = \sqrt{\frac{\eta}{|\alpha_2|}}\sqrt{\frac{\lambda-1}{\lambda+1}}, \quad (41)$$

where σ is a material constant of order one. The inversion wall thickness $\xi = \sigma\cdot\ell_f$ is inversely proportional to the shear rate. An inversion wall solution to this steady sine-Gordon equation [58], for $\varphi=0$ at $y=-\infty$, and $\varphi=\pi$ at $y=+\infty$, and whose midplane is located at $y=y_0$ is

$$\tan\frac{\phi}{2} = \exp\left(\frac{(y-y_o)}{\xi}\right). \quad (42)$$

Using Eq. (1) we find that for solution (42) the topological charge of the inversion wall is $C=+1$. A positive charge corresponds to anti-clockwise rotation for increasing y. The corresponding $C=-1$ wall is

$$\tan\frac{\pi-\phi}{2} = \exp\left(\frac{(y-y_o)}{\xi}\right). \quad (43)$$

At the surfaces the director is anchored along the vorticity and inversion walls next to the surface will be called half-walls since the rotation across in only $\pi/2$ radians.

The steady sine-Gordon equation also admits soliton lattice solutions, that represent an array of inversion walls, separated by a constant period Λ. The periodic array of inversion walls, of alternating charge is given by [58]

$$\sin\left(\theta - \frac{\pi}{2}\right) = SN\left(\frac{y}{\xi\rho}, \rho\right), \quad (44a)$$

a)

b)
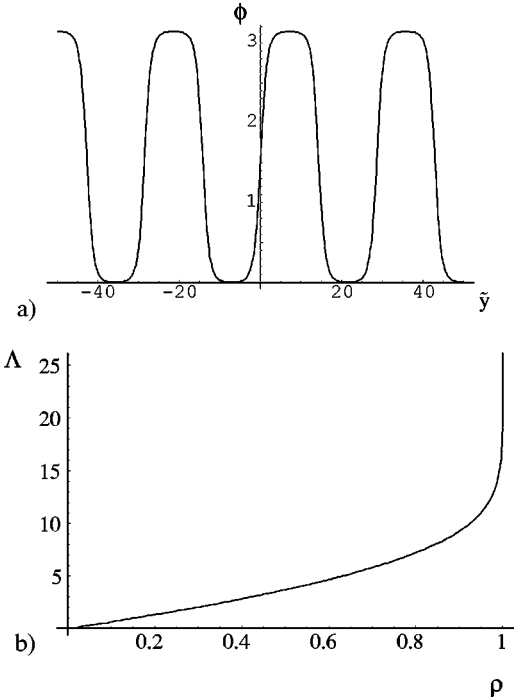
FIG. 5. (a) The twist angle as a function of $\tilde{y}=y/\xi$ for $\rho=0.9999$. (b) The period Λ as a function of the modulus ρ. As $\rho>1$, an array of inversion walls appear, whose period increases exponentially with ρ.

$$\Lambda = 4\xi\rho\Xi(\rho), \quad (44b)$$

where SN is the Jacobian elliptic function [58] of modulus ρ, and Λ is the distance between walls. Figure 5(a) shows the twist angle as a function of $\tilde{y}=y/\xi$ for $\rho=0.9999$, and Fig. 5(b) the period Λ as a function of the modulus ρ. As $\rho>1$, an array of inversion walls appear, whose period increases exponentially with ρ. The number of walls in a shear cell of thickness H is $N(\rho)=H/\Xi(\rho)$.

We have shown that when Er is high enough the nonhomogenous modes exhibit the following inversion wall phenomena. (a) Symmetric mode (S): there are two half-walls at the bounding surface. The net charge is always zero. If the top surface has $C=-1/2$ the bottom surface has a charge $C=+1/2$. (b) Antisymmetric mode (AT): there are three walls. The net charge is always zero. The surfaces have equal charge. (c) Defect lattice mode (DL): there are n walls. The original net charge is zero. Since, as shown below, wall coarsening and pinching processes take place in this mode, and since charge is not conserved, the net charge when coarsening and pinching occur has to be computed.

C. Wall interactions and coarsening phenomena

Coarsening processes of inversion walls under shear can involve (a) pinching [4], (b) a wall-bounding surface reaction, and (c) wall-wall annihilation. Wall pinching eliminates an inversion wall by nucleating a defect pair, and will be discussed in the next section since it involves spatial changes in the scalar order parameter S. Wall-surface reactions and wall-wall annihilation are driven by a decrease in the energy

of the system. As in other defects, the topological charge in these two processes is conserved:

$$C_i + C_j \Rightarrow C_{i+j}, \qquad (45)$$

where the subscript is the charge of the wall in the bulk or at the bounding surface. Recall that at the bounding surfaces all nonhomogeneous modes have an inversion wall. When the tails of two neighboring walls come into contact, the forces of attraction between the walls drive the interaction leading to a decrease in the number of walls. To estimate the force of attraction between walls in these two coarsening processes we derive a dynamical free energy per unit area F_a associated with Eq. (40):

$$F_a = \dot{\gamma}|\alpha_2|\sin\theta_L \int_0^\Lambda \left[\frac{\xi^2}{2}\left(\frac{d\phi}{dy}\right)^2 + \cos\phi \right] dy. \qquad (46)$$

For a train of inversion walls [soliton lattice solution (44a)], the integrand is a positive constant B greater than 1 ($B > 1$) [58]:

$$\frac{\xi^2}{2}\left(\frac{d\phi}{dy}\right)^2 + \cos\phi = B, \qquad (47)$$

whose magnitude is related to the modulus ρ and hence to the wall-wall separation distance $\Lambda = 4\xi\rho\Xi(\rho)$ as follows [58]:

$$B = 1 + \frac{2}{\rho^2}(1-\rho^2). \qquad (48)$$

The force of attraction per unit area Γ between two oppositely charged walls is then

$$\Gamma = -\frac{dF_a}{d\Lambda} = -\dot{\gamma}|\alpha_2|\sin\theta_L B. \qquad (49)$$

Below we show that the simulations predict that in a range of Ericksen numbers, wall-wall and wall-surface coarsening processes driven by attractive interactions take place.

IV. NUMERICAL RESULTS AND DISCUSSION

We next classify, characterize, and discuss the numerical solutions to Eqs. (17), obtained using the auxiliary data (27). All transient results are shown as a function of strain: $\gamma = \dot{\gamma}t$.

A. Classification of steady state solutions

In this section we present the main characteristics of the six type of steady state solutions predicted by the Landau–de Gennes equations, for initial conditions and boundary conditions along the vorticity direction. As shown above, the LE equations predict the existence of four stable steady state modes. On the other hand, we find that as the Ericksen number increases the Landau–de Gennes equations predict the existence of two additional stable steady state modes, as follows: (a) homogeneous mode (H), (b) symmetric mode (S), (c) antisymmetric mode (AT), (d) defect lattice mode (DL),

(e) defect gas mode (DG), and (f) planar mode (P). The complete characterization of the six modes includes (1) the symmetry of the twist angle profile, $\varphi(y^*)$, (2) the net topological charge C, and (3) the layer periodicity in the presence of multiple walls. The additional two modes for the Landau–de Gennes equations arise because scalar order changes at sufficiently high De introduce coarsening by pinching processes.

Figure 6 shows the complete characterization of all the stable steady state solutions to Eq. (17) with auxiliary data (27), including representative computed visualizations, symmetry properties of the twist angle profile, net topological charge due to the presence of inversion walls, and periodicity in the presence of an array of walls. The representative computed visualizations of the director field are for $R = 10^5$. The dark dots represent the inversion walls. By increasing the Ericksen number the following director symmetry transition cascade is observed: symmetric→antisymmetric →symmetric or antisymmetric→asymmetric→symmetric or antisymmetric. In terms of net charge the transition cascade is: $C=0 \rightarrow C=0, \pm n(n=1,2...) \rightarrow C=0, \pm 1$. In terms of the periodicity in the defect modes, the transition cascade is: monotonic→periodic→defect aperiodic→monotonic. The values of transition Ericksen numbers are (for $R=10^5$) approximately. $\mathrm{Er_{HS}}=70$, $\mathrm{Er_{SA}}=10^3$, $\mathrm{Er_{ADL}}=9\times10^3$, $\mathrm{Er_{DLDG}} =1.2\times10^5$, and $\mathrm{Er_{DLP}}=1.8\times10^5$, where the subscript indicate the two modes involved in the transition: HS; homogeneous-symmetric; SA, symmetric-asymmetric; ADL, asymmetric-defect lattice; DLDG, defect lattice-defect gas; DGP, defect gas-planar. The interval between two successive critical Ericksen and Deborah numbers defines the basin of attraction of the shown mode. The main differences between the LE defect lattice mode obtained with the one constant approximation and fixed alignment angle approximations (see Eq. (44a)] and the computed Landau–de Gennes defect mode is that the former is periodic [see Eq. (44b) for the period Λ] with zero net charge ($C=0$), while the latter exhibits weak deviations from perfect periodicity, although the net charge is zero because no coarsening process has taken effect. The weak deviations from periodicity in the predicted Landau–de Genned solutions arise because of the elastic anisotropy ($K_{22} \neq K_{11} = K_{33}$) and because the equations are fully coupled; this weak deviation is not significant in the description of the essence of this mode, and hence we retain the defect lattice label. Since as mentioned above the Landau–de Gennes equations converge into the LE equations [with $K_{11}=K_{33}$ when using Eq. (29)] the first four modes (i.e., H-S-AT-DL) are predicted by both theories. As Er increases and De becomes closer to 1, wall pinching processes emerge, and the solutions of both models diverge, and the last two modes are only predicted by the Landau–de Gennes model. Hereafter we concentrate on the prediction of the Landau–de Gennes model since it allows for shear-induced textural transformations. The defect gas and planar modes that occur at higher Ericksen numbers are the result of defect coarsening process. Since in one-dimensional simulations pinching extinguishes a wall without a defect pair nucleation, the net topological charge in the defect gas after wall pinching is undetermined. In addition since coarsening

Solution Type	Homogeneous H	Symmetric S	Antisymmetric AT	Defect Lattice DL	Defect Gas DG	Planar P
Visualizations						
Basin of Attractions	Er=0 → Er$_{HS}$=70 0 → De=De$_{HS}$=7x10^{-5}	Er$_{HS}$ → Er$_{SA}$=10^3 De$_{HS}$ → De$_{SA}$=10^{-3}	Er$_{SA}$ → Er$_{ADL}$=9x10^3 De$_{SA}$ → De$_{ADL}$=9x10^{-3}	Er$_{ADL}$ → Er$_{DLDG}$=1.2x10^5 De$_{ADL}$ → De$_{DLDG}$=1.2	Er$_{DLDG}$ → Er$_{DGP}$=1.8x10^5 De$_{DLDG}$ → De$_{DGP}$=1.8	Er > Er$_{DGP}$ De > De$_{DGP}$
Symmetry	NA	Symmetric	Antisymmetric	Symmetric or Antisymmetric	Asymmetric	Symmetric or Antisymmetric
Net Charge	0	0	0	0	0, ± n (n=1,2,...)	0, ± 1
Periodicity	NA	NA	Periodic	Periodic	Aperiodic	NA

FIG. 6. Characterization of all the stable steady state solutions to Eqs. (17) with auxiliary data (27), including representative computed visualizations, symmetry properties of the twist angle profile, net topological charge due to the presence of inversion walls, and periodicity in the presence of an array of walls, for $R = 10^5$. The dark dots represent the inversion walls. By increasing the Ericksen number the following director symmetry transition cascade is observed: symmetric→antisymmetric→symmetric or antisymmetric→asymmetric →symmetric or antisymmetric. In terms of net charge the transition cascade is $C = 0 → C = 0, ± n (n = 1,2...) → C = 0, ± 1$. In terms of texture, unoriented monodomain→defect lattice→defect gas→oriented monodomain. The values of transition Ericksen numbers are (for $R = 10^5$) approximately: Er$_{HS}$ = 70, Er$_{SA}$ = 10^3, Er$_{ADL}$ = 9 × 10^3, Er$_{DLDG}$ = 1.2 × 10^5, and Er$_{DLP}$ = 1.8 × 10^5, where the subscript indicate the two modes involved in the transition. HS: homogeneous-symmetric; SA: symmetric-asymmetric; ADL: asymmetric-defect lattice; DLDG: defect lattice-defect gas; DGP: defect gas-planar.

by wall-wall annihilation takes places, the periodicity of the defect lattice is destroyed. The high shear rate planar mode differs from the low shear rate symmetric mode in that the symmetry and charge are undetermined, since the planar mode is the result of multiple pinching processes. Since the objective of this paper is the characterization of textural transformation under shear we restrict the discussion to the defect lattice, defect gas, and planar modes.

Figure 7(a) shows the steady state twist ϕ and tilt θ angles as a function of dimensionless distance y^*, for $R = 10^5$, Er $= 7 \times 10^4$ (De = 0.7). The figure represents typical angles profiles for the defect lattice (DL) mode, with two inversion walls in the bulk. At these relatively low Er no coarsening takes place, the net charge is zero, and the director is periodic. Figure 7(b) shows the steady state twist ϕ and tilt θ angles as a function of the dimensionless distance y^*, for $R = 10^5$, and Er $= 1.2 \times 10^5$ (De = 1.2). The figure represents typical angles profiles for the defect gas (DG) mode, with five inversion walls. At these relatively high Er coarsening took place, the net charge is not zero, and the director is aperiodic. In this particular case the net charge is zero.

B. Shear-induced texture coarsening mechanisms

The steady state texture of a liquid crystal is given by the balance of nucleation and coarsening processes. Coarsening events limit the lifetime of an inversion wall, and a texture can be viewed as a balance between birth-death events in the regime that leads to the defect gas and planar modes. In this section we characterize the following texture coarsening processes: (a) wall-wall annihilation (mode WW), (b) a wall-bounding surface reaction (mode WS), and (c) wall pinching (mode WP). We also characterize the dependence of the coarsening process on the governing length and time scale ratios R, Er, and De. Since the governing time scales at high shear rates are the flow time scale [see Eq. (24)], all transient results are plotted as a function of strain $\gamma = \dot{\gamma}t$. Although De and Er are related by Eq. (21), below we emphasize their distinct role.

Figure 8(a) shows a computed gray scale visualization of director component n_z ($0 \leq y^* \leq 1$) as a function of strain, for $R = 10^4$, De = 1.2 (Er $= 1.2 \times 10^4$), corresponding to wall-wall interaction in the planar (P) mode. Black represents an in plane orientation ($n_z = 0$) and light represents an orienta-

a)

b)
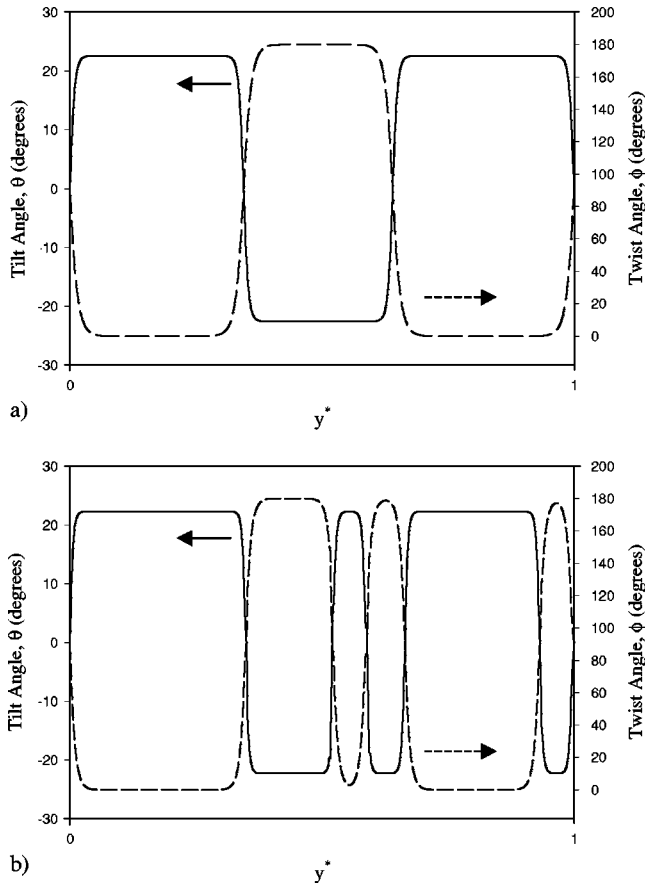
FIG. 7. (a) Steady state twist ϕ and tilt θ angles as a function of dimensionless distance y^*, for $R=10^5$ Er$=7\times10^4$ (De$=0.7$) for the defect lattice (DL) mode, with two inversion walls in the bulk. At these relatively low Er no coarsening takes place, the net charge is zero, and the director is periodic. (b) The steady state twist ϕ and tilt θ angles as a function of dimensionless distance y^*, for $R=10^5$, and Er$=1.2\times10^5$ (De$=1.2$), for the defect gas (DG) mode, with five inversion walls. At these relatively high Er coarsening took place, the net charge is not zero, and the director is aperiodic.

tion along the vorticity ($n_z=1$) axis. For $\gamma<70$ there are two oppositely charged inversion walls in the bulk. As strain increases the walls annihilate,

$$C_{+1}+C_{-1}\Rightarrow0, \tag{50}$$

leaving behind a planar director field. The figure shows a manifestation of the attractive interaction between oppositively charged walls [see Eq. (50)]. Figure 8(b) shows a computed gray scale visualization of director component n_z ($0\leqslant y^*\leqslant1$) as a function of strain for $R=10^4$ and De$=1.8$ (Er$=R$De$=1.8\times10^4$), corresponding to wall pinching in the planar mode. Black represents in plane orientation ($n_z=0$) and light orientation along the vorticity ($n_z=1$). For $\gamma<50$ there are two oppositely charged inversion walls in the bulk. As strain increases the walls pinch separately,

$$C_{+1}\Rightarrow0,\quad C_{-1}\Rightarrow0, \tag{51}$$

leaving behind a planar director field. Since two walls disappear in this case, the net charge is conserved. The figure

shows a manifestation of molecular elasticity represented by De. When the flow is strong enough, the scalar order parameter changes since flow time scales are faster than scalar order parameter time scales, and new coarsening routes appear. Figure 8(c) shows an order parameter S visualization corresponding to Fig. 8(b). Light corresponds to $S=S_{eq}=0.68$ [see Eq. (27)] and black to $S=0$. When the walls pinch S at the center of the wall decreases to zero, leaving behind a planar field. Figure 8(d) shows a computed gray scale visualization of director component n_z ($0\leqslant y^*\leqslant1$) as a function of strain for $R=10^6$, De$=0.9$ (Er$=R$De $=9\times10^5$), corresponding to wall-bounding surface interaction in the defect lattice mode. Black represents in plane orientation ($n_z=0$) and light orientation along the vorticity ($n_z=1$). For $\gamma<80$ there are two oppositely charged inversion walls in the bulk. As the strain increases one wall is absorbed by the bounding surface.

$$C_{-1}+C_{1/2}\Rightarrow C_{-1/2}, \tag{52}$$

leaving behind a single wall in the bulk. The figure shows a manifestation of the attractive interaction between oppositely charged walls [see Eq. (52)]. In this case charge is conserved since the charge of the lower bounding surface changes from $+1/2$ before the absorption to $-1/2$ afterwards. Figure 8(d) is a unique example of a defect-bounding surface interaction. Models of surface defect emission have been postulated [43], and also observed experimentally [26] but never simulated with the classical nematodynamics equations.

C. Shear-induced defect nucleation and coarsening mechanisms and texture scaling

Next we characterize the dependence of defect nucleation rates and coarsening rates as a function of the time and length scales ratios Er, R, and De. For efficiency we refer to the three coarsening processes (WW, WS, WP), and to wall nucleation as defect events. The number of coarsening events is denoted $\mathbb{C}$. The number of nucleation events is denoted by $\mathbb{N}$.

Figure 9 shows the total number of nucleated walls during dynamical simulations as a function of the Ericksen number, for R: (a) 10^4, (b) 10^5, and (c) 10^6. At sufficiently high R, a power law regime emerges. For $R=10^6$ and Er$>$Er$_{ADL}$, the simulation results are the fitted curve using a power law model:

$$\mathbb{N}=\varepsilon\Upsilon(\text{Er}-\text{Er}_{ADL})\sqrt{\text{Er}-\text{Er}_{ADL}}, \tag{53}$$

where Υ is the Heaviside function. The corresponding values of the amplitude $\varepsilon=0.0147$ for $R=10^6$. In terms of length scales the power law scaling gives, for Er$>$Er$_{ADL}$,

$$H=\ell_f\mathbb{N}\sqrt{1+\frac{\text{Er}_{ADL}}{\mathbb{N}}}\approx\xi\mathbb{N}\sqrt{1+\frac{\text{Er}_{ADL}}{\mathbb{N}}}, \tag{54}$$

where we used Eqs. (41) and (53). The asymptotic regimes are

$$\mathbb{N}<\sqrt{\text{Er}_{ADL}},\quad H\approx\xi\text{Er}_{ADL}, \tag{55a}$$
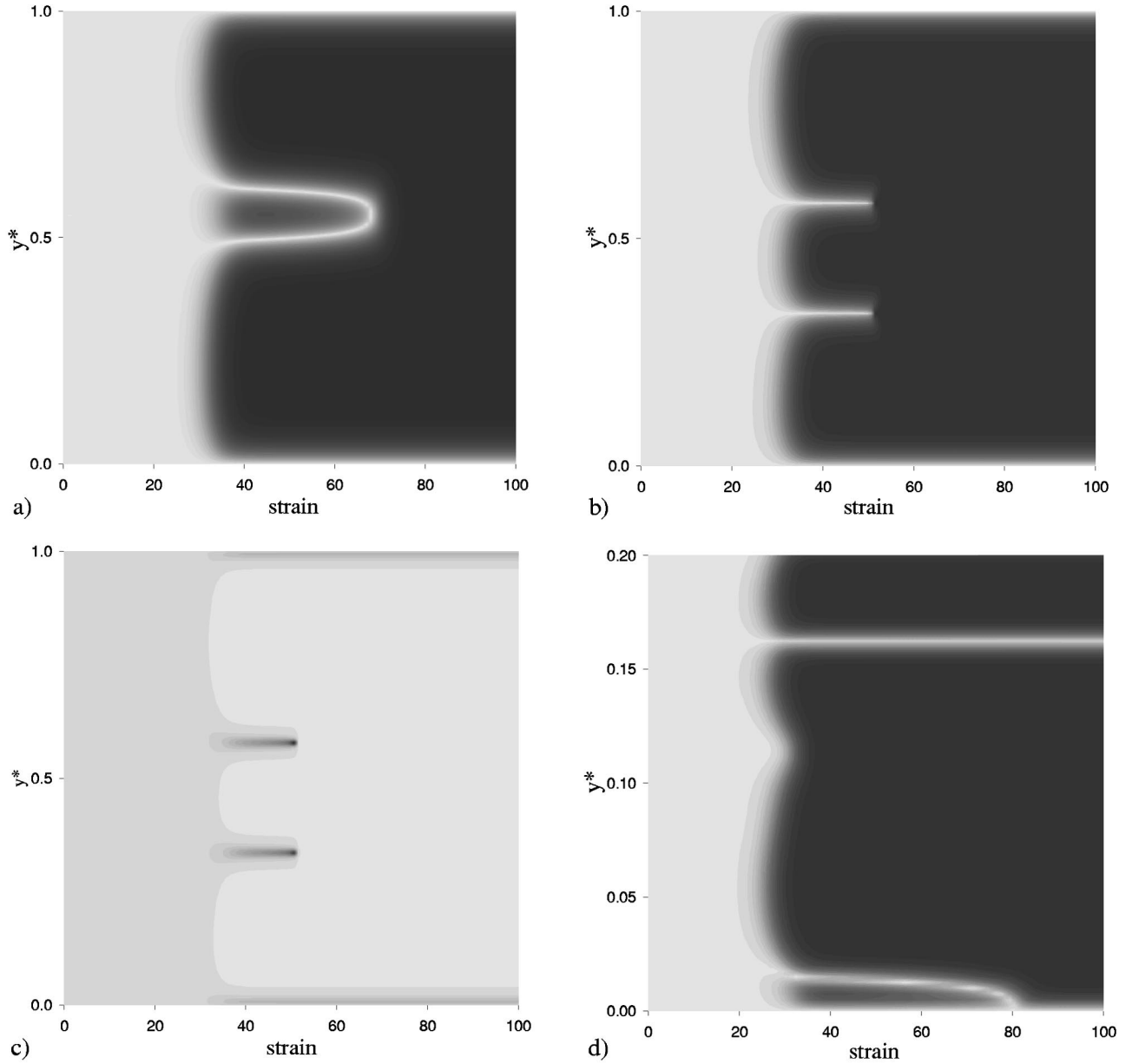
FIG. 8. Computed gray scale visualization of director component n_z $(0 \leqslant y^* \leqslant 1)$ as a function of strain. Black represents in plane orientation $(n_z = 0)$ and light orientation along the vorticity $(n_z = 1)$: (a) wall-wall interaction in a planar mode, $\mathrm{Er} = 1.2 \times 10^4$, $R = 10^4$. (b) Wall pinching in a planar mode, $\mathrm{Er} = 1.8 \times 10^4$, $R = 10^4$. (c) The order parameter S visualization corresponding to (b). Light corresponds to $S = S_{\mathrm{eq}} = 0.68$ and black to $S = 0$. When the walls pinch, the order parameter S at the center of the wall decreases to zero, leaving behind a planar field. (d) Wall-bounding surface interaction in the defect lattice mode, $\mathrm{Er} = 9 \times 10^5$, $R = 10^6$.

$$\mathbb{N} > \sqrt{\mathrm{Er}_{\mathrm{ADL}}}, \quad H \approx \xi \mathbb{N}. \tag{55b}$$

The length scale of the texture $\ell_t = H/\mathbb{N}$ is given by

$$\ell_t = \frac{H}{\varepsilon \Upsilon (\mathrm{Er} - \mathrm{Er}_{\mathrm{ADL}}) \sqrt{\mathrm{Er} - \mathrm{Er}_{\mathrm{ADL}}}}. \tag{56}$$

Thus in the absence of coarsening the texture length scale decreases with a $-\frac{1}{2}$ power law.

Figure 10 shows the total number of coarsening events $\mathbb{C}$ during the dynamic simulations, as function of the Deborah number for R: (a) $R = 10^4$, (b) $R = 10^5$, and (c) $R = 10^6$. For all R the most significant mechanism is wall pinching. As R increases the rate of pinching $\mathbb{R}_C$ increases rapidly with De. The computations show for De > 1, the the coarsening process follows a power law:

$$\mathbb{C} = \chi (\mathrm{De} - \mathrm{De}_{\mathrm{DLDG}})^n \tag{57}$$

with $\chi = 29.3$ and $n \approx 1$. For large $R = 10^6$ the figure shows that pinching starts at $\mathrm{De}_{\mathrm{DLDG}} \approx 1$. This condition implies, using Eq. (21), that $\mathrm{Er} \approx R$. This equality implies the following equality of length scales:

a)

b)

c)
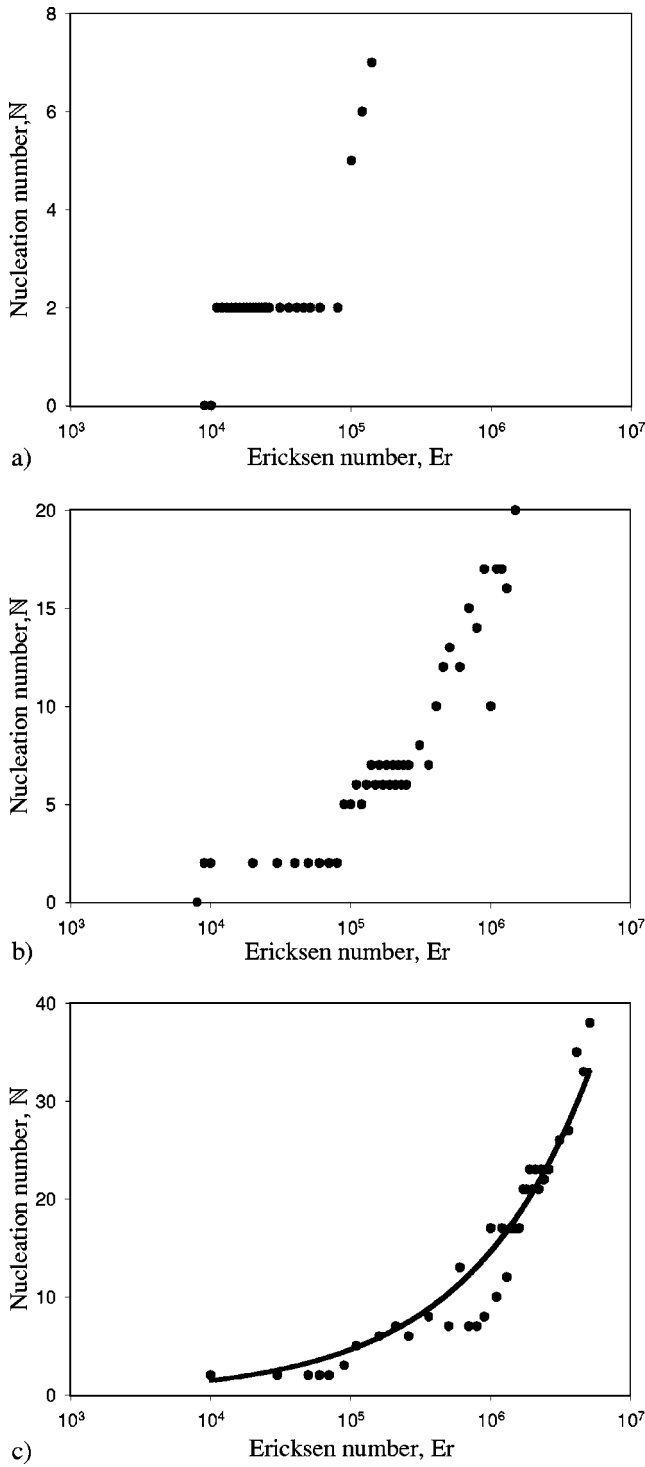
FIG. 9. Number of nucleated walls during dynamical simulations as a function of the Ericksen number, for R: (a) 10^4, (b) 10^5, and (c) 10^6. At sufficiently high R, a power law regime emerges. The points are the simulation results and the solid lines are the fitted curve using a power law model (58). The amplitude is $\varepsilon = 0.0147$.

$$\text{Er} \approx R \Rightarrow \frac{H^2}{\ell_f^2} \approx \frac{H^2}{\ell_i^2} \Rightarrow \ell_f \approx \ell_i . \tag{58}$$

Thus when the flow length scale is close to the internal

a)

b)

c)
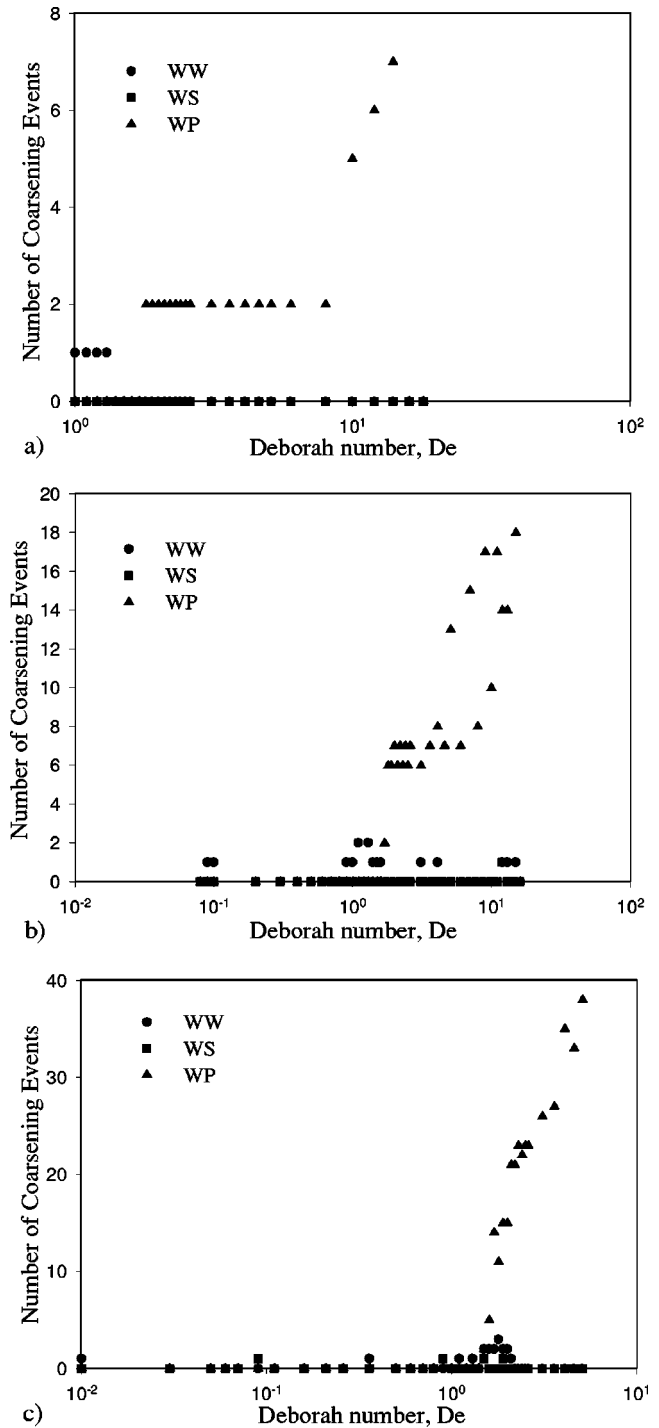
FIG. 10. Total number of coarsening events $\mathbb{C}$ during the dynamic simulations, as a function of the Deborah number for R: (a) $R = 10^4$, (b) $R = 10^5$, and (c) $R = 10^6$. For all R the most significant mechanism is wall pinching. As R increases the rate of pinching $\mathbb{R}_C$ increases rapidly with De.

length scale pinching occurs. Since the flow scale is the wall thickness we also find that pinching occurs when $\xi \approx \ell_i$.

Figure 11 shows the total number of nucleation and annihilation events during the dynamic simulations, as a function of the Deborah number De for R: (a) $R = 10^4$, (b) $R = 10^5$, and (c) $R = 10^6$. The figure shows the existence of three re-
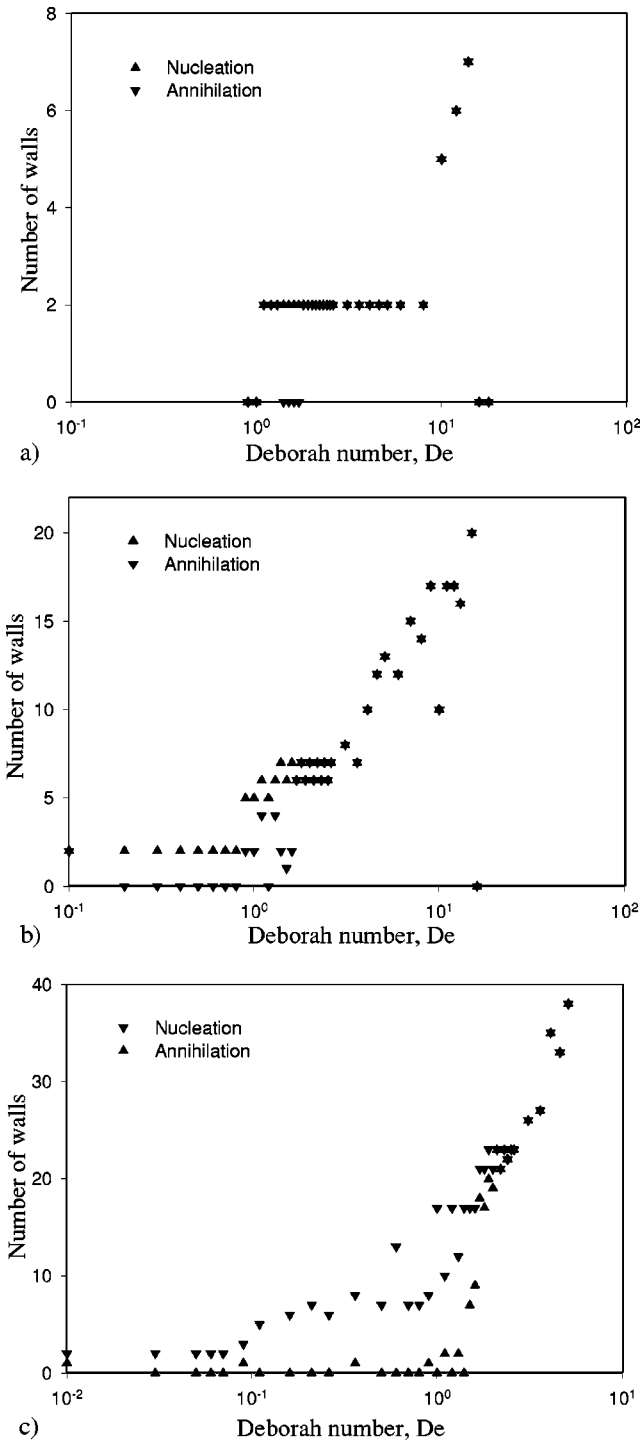
FIG. 11. Total number of nucleation and annihilation events during the dynamic simulations, as function of the Deborah number for R: (a) $R = 10^4$, (b) $R = 10^5$, and (c) $R = 10^6$. The figure shows the following dependences. De <1: nucleation rate $>$ annihilation rate, $N_{ss} > 0$; De $\approx 1 - 2$: nucleation rate $\approx$ annihilation rate, $N_{ss} > 0$; De >2: nucleation rate = annihilation rate, $N_{ss} = 0$.

gimes: (a) Defect nucleation (Er $\gg 1$, De <1): $\mathbb{N} > \mathbb{C}$, $N_{ss} > 0$. (b) Defect nucleation and defect coarsening (De $\approx 1 - 2$): $\mathbb{N} > \mathbb{C}$, $N_{ss} > 0$. (c) Defect coarsening (De >2): $\mathbb{N} = \mathbb{C}$, $N_{ss} = 0$. N_{ss} is the number of walls at the steady state. The indicated critical De for each regime correspond to R

$\approx 10^6$ but for lower R small adjustments of order 1 occur. In the defect nucleation regime the length scale ordering is $H \ll \ell_f \approx \ell_i$, and walls nucleate but do not pinch. In the intermediate nucleation-coarsening regime the length scale ordering is $H \ll \ell_f \sim \ell_i$, and thus nucleation and pinching occur at similar rates. Finally, in the coarsening regime, $H \ll \ell_i > \ell_f$, and pinching becomes equal with the nucleation. Note that since $\ell_f \approx \xi$ [see Eq. (58)] when the wall thickness ξ is smaller than the internal length scale ℓ_i, walls pinch.

Figure 12 shows a gray-scale plots of the out-of plane director component n_z as a function of strain γ, for $R = 10^5$; $n_z = 1$ corresponds to white and $n_z = 0$ to black, for the following De (Er): (a) 1.2 (1.2×10^5), (b) 1.6 (1.6×10^5), and (c) 2 (2×10^5), representative of the defect gas and planar modes. In Fig. 12(a) five inversion walls nucleate but since De $=1.2$ and $R = 10^5$, there is no annihilation, and the net charge is zero. In Fig. 12(b), De $=1.6$ there is one wall-wall annihilation (WW) event, leaving behind a defect gas mode with zero topological charge. In Fig. 12(c) seven inversion walls nucleate but since De $=2$ seven pinching (WP) events take place, leaving behind a planar mode.

Figure 13(a) shows the number of inversion walls as a function of strain corresponding to Fig. 12. Figure 13(b) shows the corresponding total dimensionless long range free energy as a function of strain, computed by integrating the dimensionless free energy density given in Eq. (9). For the higher Er condition, the dimensionless long range energy function illustrates the existence of three temporal regions. (a) Early stage ($\gamma < 30$): the out-of-plane orientation and the long range energy are close to zero. (b) Intermediate stage: nucleation of walls and an increase of long range energy. (c) Late stage: coarsening by annihilation and a steplike energy decrease. Each wall that disappears produces an energy step decrease. For low Er the response is sigmoidal since no coarsening takes place. For the highest Er the response is a pulse since coarsening has been eliminated all the walls.

Figure 14(a) shows a gray scale plot of the out-of plane director component n_z as a function of strain for $R = 10^6$ and De $=12$ (Er $=1.2 \times 10^7$). When De >1, the number of walls increase [in accord with Eq. (44b)] (Er $=1.6 \times 10^7$). At sufficiently high De (De $\cong 16$) the layered structure is replaced by a homogeneously aligned system [Fig. 14(b)]. The figures show that as De increases the pinching occurs at smaller and smaller strains.

D. Shear-induced texture formation

Models and mechanisms for shear-induced texture formation have been investigated experimentally [17] but are not well understood theoretically. Here we refer to the texture as the density of defects; the only defects in our one-dimensional simulations are inversion walls. The long standing issue of interest is what mechanisms contribute to the nucleation and coarsening processes of textures. The prediction of a shear-induced defect mode by the classical models of nematodynamics provides insights into these questions. In this section we characterize the parametric dependence of the defect mode length scale as a function of the governing ra-
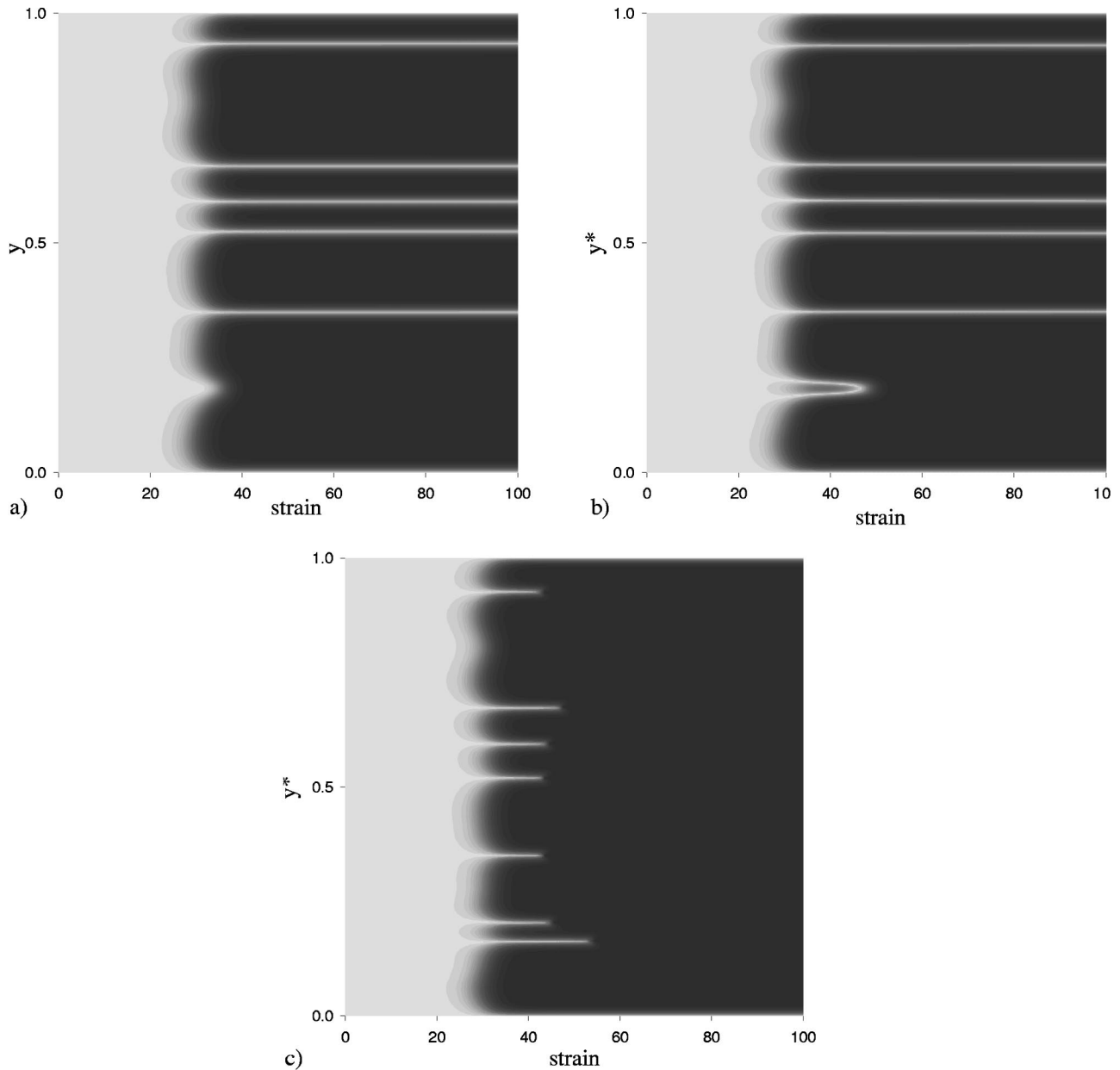
FIG. 12. Gray-scale plots of the out-of plane director component n_z as a function of strain, for $R = 10^5$; $n_z = 1$ corresponds to white and $n_z = 0$ to black, for the following Er: (De) (a) 1.2×10^5 (1.2), (b) 1.6×10^5 (1.6), and (c) 2×10^5 (2), representative of the defect gas and planar modes.

tios of time and length scales: R, Er, and De. To characterize the steady state texture length scale ℓ_t under shear we use its reciprocal, or the number of inversion walls at steady state N_{ss}.

Figure 15(a) shows the number of inversion walls N_{ss} at steady state as a function of the Ericksen number for R, 10^4, 10^5, 5×10^5, and 10^6, corresponding to the defect modes. The figure shows that as R increases the number of walls increases. The figure establishes that the appearance of the defect modes is only a function of Er, but is independent of R. The figure shows that when $\mathrm{Er} < \mathrm{Er}_{ADL} \approx 10^4$ no walls are observed for all values of R. The maximum number of walls depends on R and Er. For example, for $R = 10^6$, 17 walls are

found at $\mathrm{Er} = 10^6$, but for $R = 10^5$ only five walls emerge at $\mathrm{Er} = 10^5$. Figure 15(b) shows the number of inversion walls N_{ss} at steady state as a function of the Deborah De number for R: 10^4, 10^5, and 10^6. The maximum number of walls occurs at $\mathrm{De} \cong 1$ and the upper threshold of the defect gas mode is $\mathrm{De}_{DGP} \cong 2$ for all values of R. The figures show that the texture behavior (i.e., number of walls) for $\mathrm{De} < 1$ is controlled by the Ericksen number while for $\mathrm{De} \geq 1$ it is controlled by the Deborah number. Furthermore for $\mathrm{De} > 2$, textural features are eliminated and a monodomain (planar mode) emerges. The computational results shown in Figs. 15 can be rationalized and approximated by the power law behavior explained in conjunction with Eqs. (53) and (57), as

a)

b)
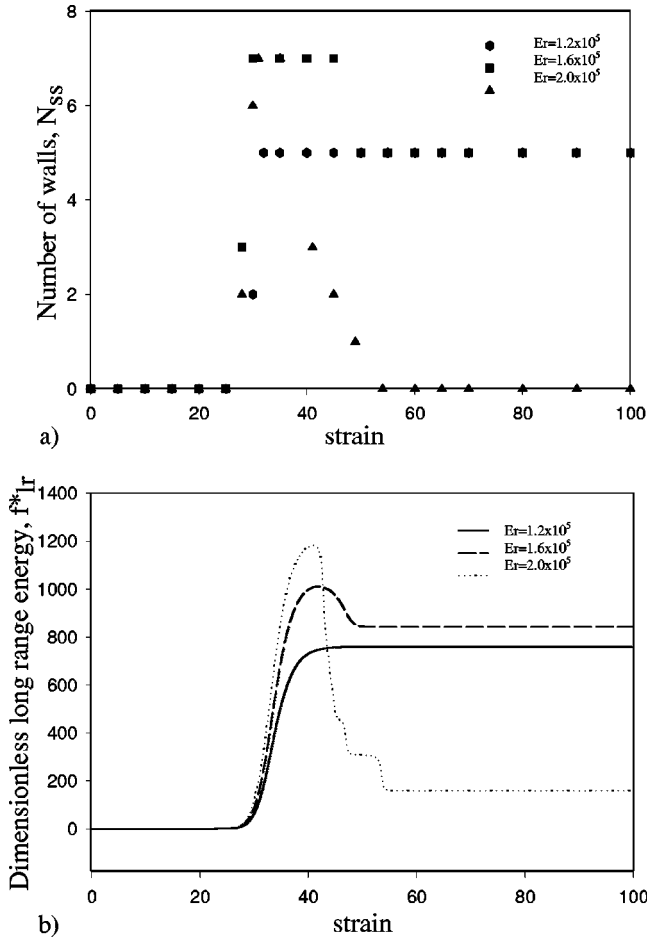
FIG. 13. (a)Number of inversion walls as a function of strain for the same values of E_r number and R as in Fig. 12. (b) Total dimensionless long range free energy as a function of strain γ, computed by integrating the dimensionless free energy density given in Eq. (9). The dimensionless long range energy function illustrates the existence of three temporal regions: early stage ($\gamma < 30$), the out-of-plane orientation and the long range energy are close to zero; intermediate stage; nucleation of walls and increase of long range energy; and late stage; coarsening by annihilation and steplike energy decrease. Each wall that disappears produces an energy step decrease.

a)

b)

FIG. 14. Gray-scale plots of the out-of plane director component n_z as a function of strain, for ($n_z = 1$ corresponds to white and $n_z = 0$ to black). (a) $R = 10^6$, De $= 12$ (Er $= 1.2 \times 10^7$). (b) $R = 10^6$, De $= 16$ (Er $= 1.6 \times 10^7$). When De > 1, the number of walls increase [according to Eq. (44)] (Er $= 1.6 \times 10^7$). At sufficiently high De (De $\cong 16$) the defect gas is replaced by a homogeneously aligned system (b).

follows. In terms of the De number, the number of walls N_{ss} at steady state is given by

$$N_{ss} = \mathbb{N} - \mathbb{C}. \tag{59}$$

Using the power law results we find, for De $\leq$ De$_{DGP}$,

$$N_{ss} = \underbrace{\varepsilon \Upsilon (R\text{De} - \text{Er}_{ADL}) \sqrt{R\text{De} - \text{Er}_{ADL}}}_{\text{nucleation}}$$

$$\underbrace{- \Upsilon (\text{De} - \text{De}_{DLDG}) \chi (\text{De} - \text{De}_{DLDG})^n}_{\text{coarsening}} \tag{60}$$

indicating that the nucleation growth scales with $\sqrt{\text{De}}$ and is weaker than the coarsening rate, which scales with $(\text{De})^n$, and $n \approx 1$. For De $>$ De$_{DGP}$, the number of walls is $N_{ss} = 0$.

Using Eq. (60), with $n = 1$, we find that the maximum number of walls N_{ssmax} is

$$N_{ssmax} = \varepsilon \sqrt{R\text{De}_{DLDG} - \text{Er}_{ADL}}, \quad R\text{De}_{DLDG} > \text{Er}_{ADL}. \tag{61}$$

The inversion walls vanish ($N_{ss} = 0$) at the upper critical Deborah number De$_{DGP}$:

$$\varepsilon \sqrt{R \mathrm{De}_{\mathrm{DGP}} - \mathrm{Er}_{\mathrm{ADL}}} = \chi(\mathrm{De}_{\mathrm{DGP}} - \mathrm{De}_{\mathrm{DLDG}}) \Rightarrow \mathrm{De}_{\mathrm{DGP}}$$

$$\approx \mathrm{De}_{\mathrm{DLDG}}^2, \tag{62}$$

where we used the fact that $R \gg 1$, and assumed that $\mathrm{De}_{\mathrm{DGP}} \gg \mathrm{De}_{\mathrm{ADL}}$. The scaling predicts that, for large R, $\mathrm{De}_{\mathrm{DGP}}$ is independent of R, in agreement with computations. For $R = 10^6$, we find that when $\mathrm{De}_{\mathrm{DLDG}} = 1.4$ the scaling predicts $\mathrm{De}_{\mathrm{DGP}} = 1.96$ and the computations give $\mathrm{De}_{\mathrm{DGP}} = 2.1$.

$$\ell_t = \frac{H}{\varepsilon \Upsilon(\mathrm{Er} - \mathrm{Er}_{\mathrm{ADL}}) \sqrt{\mathrm{Er} - \mathrm{Er}_{\mathrm{ADL}}} - \Upsilon(\mathrm{De} - \mathrm{De}_{\mathrm{DLDG}}) \chi(\mathrm{De} - \mathrm{De}_{\mathrm{DLDG}})}, \tag{63}$$

where we wrote the nucleation in terms of Er and the coarsening in terms of De. The smallest texture length scale is

$$\ell_t = \frac{H}{\varepsilon \sqrt{\mathrm{Er}_{\mathrm{DLDG}} - \mathrm{Er}_{\mathrm{ADL}}}}. \tag{64}$$

Figure 17 shows the dimensionless length scale as a function of De for $R = 10^6$. The figure clearly implies that in the nucleation regime the texture refinement follows the shear rate scaling

$$\ell_t \propto \frac{1}{\sqrt{\dot{\gamma} - a}}, \tag{65}$$

while the coarsening follows

$$\ell_t \propto \frac{1}{\dot{\gamma} - b \sqrt{\dot{\gamma} - a} - c}, \tag{66}$$

where a, b, and c are constants. The characteristic length scale of the emerging texture is found to be in agreement with scaling proposed by Marrucci for tumbling nematics [59].

Lastly we characterize the role of the energy ratio R. Figure 18 shows the maximum number of the twist walls N_{ssmax} at steady state as a function of R. For R smaller than or equal to 10^3, our simulations predict the absence of a defect mode. The data can be fitted to a power law model (solid line), given by

$$N_{\mathrm{ssmax}} = \nu_1 \cdot \sqrt{R - \nu_2}, \tag{67}$$

where $\nu_1 = 0.017$, and $\nu_2 = 7142$. Using Eq. (61) we find that

$$N_{\mathrm{ssmax}} = \varepsilon \sqrt{\mathrm{De}_{\mathrm{DLDG}}} \sqrt{R - \frac{\mathrm{Er}_{\mathrm{ADL}}}{\mathrm{De}_{\mathrm{DLDG}}}}, \tag{68}$$

$$\nu_1 = \varepsilon \sqrt{\mathrm{De}_{\mathrm{DLDG}}}, \quad \nu_2 = \frac{\mathrm{Er}_{\mathrm{ADL}}}{\mathrm{De}_{\mathrm{DLDG}}}. \tag{69}$$

Figure 16 shows the number of walls N_{ss} as a function of the De number for $R = 10^6$, from scaling (full line) and computations (squares). The figure shows that scaling results [Eq. (60)] are in excellent agreement with the computations ($N_{\mathrm{ssmax}} = 17.33$ from scaling and 17 from the computations), and hence explain the genesis and extinction of walls in flow-aligning liquid crystal polymers.

In terms of texture length scales, Eq. (60), and $\ell_t = H/N_{\mathrm{ss}}$,

Thus increasing the energy ratio R decreases the texture length scale since the coarsening process is delayed to higher and higher shear rates.

V. DISCUSSION

Shear-induced textural transformations in flow-aligning and nonaligning low molar mass nematics, lyotropic nematic polymers, and thermotropic nematic polymers have been recently reviewed [10,18]. The most abundant experimental data on quantitative texture evolution are for nonaligning lyotropic semiflexible nematic polymers [31,32]. Since the present model captures the dynamics of flow-aligning thermotropic nematic polymers, a validation of the result with the quantitative data [31,32] is not possible.

In Refs. [31,32] samples of lyotropic liquid crystalline polymers (PBG, racemic mixture, MW: 118 000, 198 000, and 298 000) are sheared in range of Ericksen numbers [32]: $1 < \mathrm{Er} < 10^7$, with sample thickness 10–500 μm [NB: the definition of Er in Refs. [31,32] is slightly different than Eq. (20a)]. The observed textural transitions with increasing Ericksen number [31] are controlled by the Deborah number when the Deborah number approaches or exceeds unity. Using optical microscopy, the texture is characterized by the presence of stripes parallel to the flow. As shear rate increases the stripes parallel to the flow become more intense, then less intense and finally disappear at higher shear rates. The transition to the monodomain textures depends on the molecular weight (i.e., De): the higher the molecular weight the higher the shear rate necessary to eliminate the texture. Furthermore for $\mathrm{De} > 5$, textures-free samples are obtained. For a fixed geometry and set of material properties the present model predicts as the shear rate increases the texture transition cascade: unoriented monodomain $\Rightarrow$ defect lattice $\Rightarrow$ defect gas $\Rightarrow$ oriented monodomain.

VI. CONCLUSIONS

The classical theories of nematodynamics applied to thermotropic rodlike shear-flow aligning nematic polymers predict that, as the shear rate increases, the pathway between an
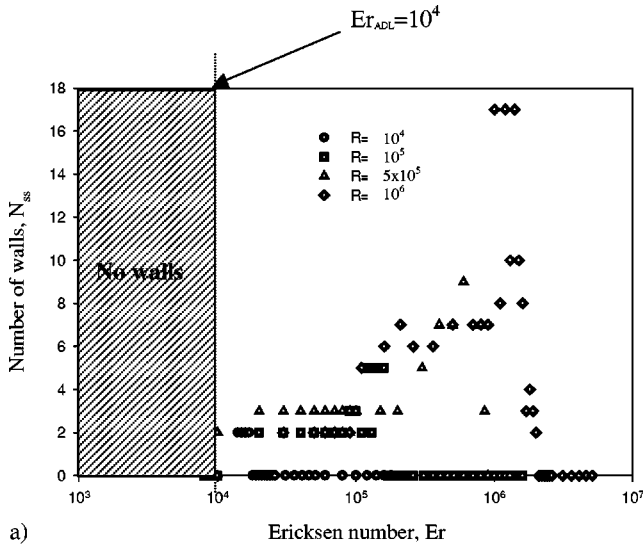
a)
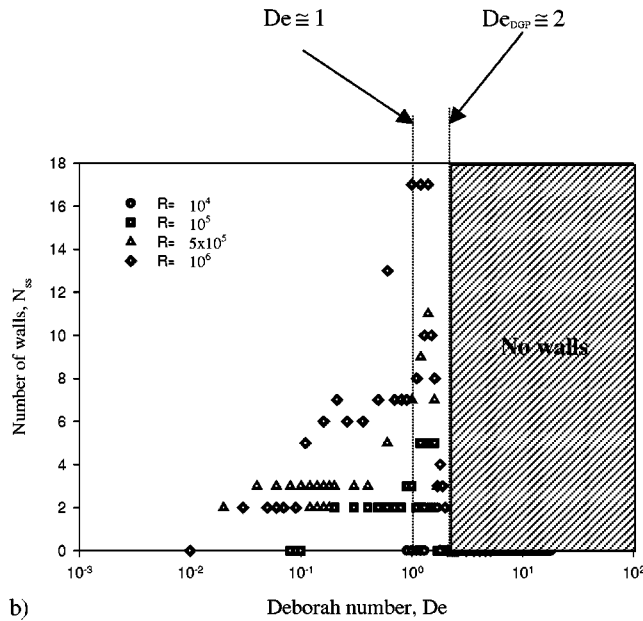
b)

FIG. 15. (a) The number of inversion walls at steady state N_{ss} as a function of the Ericksen number for R: 10^4, 10^5, 5×10^5, and 10^6, corresponding to the defect lattice and defect gas modes. As R increases the number of walls increases. The appearance of the defect modes is only a function of Er, but is independent of R. For $Er < Er_{ADL} \approx 10^4$ no walls are observed for all values of R, (b) The maximum number of inversion walls N_{ss} as a function of the Deborah De number for R: 10^4, 10^5, and 10^6. The maximum number of walls occurs at $De \cong 1$ and the upper threshold of the defect gas mode is $De_{DGP} \sim 2$ for all values of R. The texture behavior (i.e., number of walls) for $De < 1$ is controlled by the Ericksen number while for $De \geq 1$ it is controlled by the Deborah number. For $De > 2$, textural features are eliminated and a monodomain (planar mode) emerges.

oriented nonplanar state and an oriented planar state is through texture formation and coarsening. The two shear-rate dependent dimensionless numbers that control the texture formation and coarsening process are Ericksen Er and Deborah De numbers. The emergence of texture is independent of
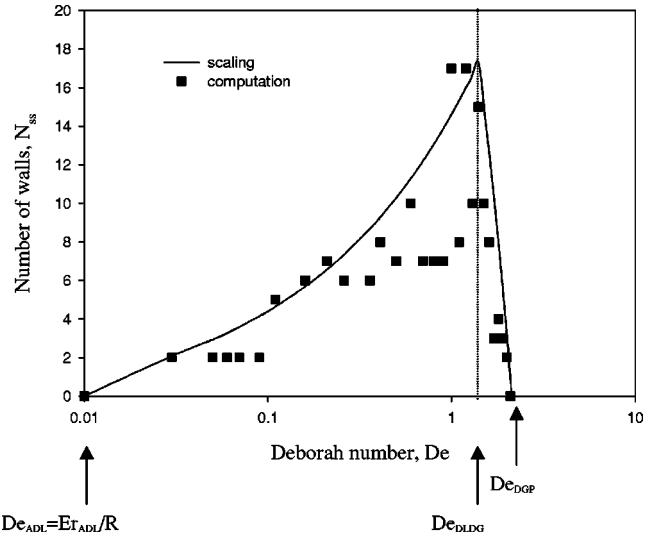
FIG. 16. The number of walls N_{ss} as a function of De number for $R = 10^6$, from scaling (full line) and computations (squares). Scaling results [Eq. (60)] are in excellent agreement with computations, and hence explain the genesis and extinction of walls in flow-aligning liquid crystal polymers.
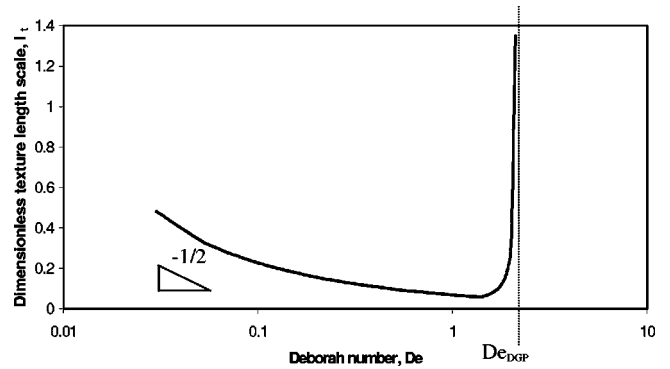
FIG. 17. Dimensionless length scale of the texture as a function of De for $R = 10^6$.
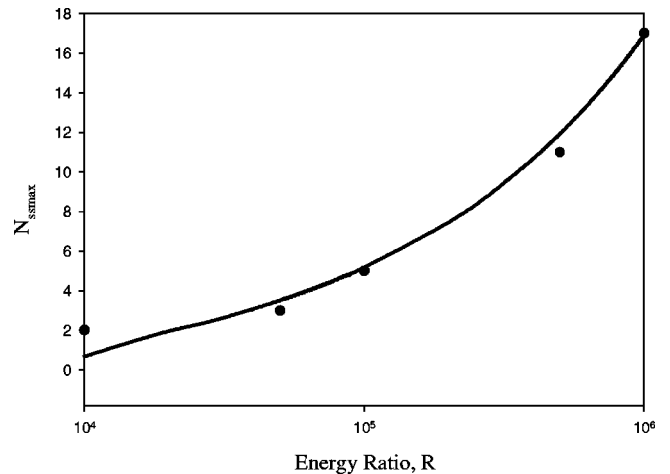
FIG. 18. Maximum number of the twist walls $N_{ss\,max}$ at steady state as a function of R. For R smaller than or equal with 1000, our simulations predict the absence of the defect mode. The data can be fitted to a power law model (solid line), given by Eq. (67), where $\nu_1 = 0.017$ and $\nu_2 = 7142$.

the Deborah number, and occurs at $Er = 10^4$. As the shear rate increases and $Er > 10^4$ the first texture that arises is a lattice of inversion walls, whose net topological charge is zero. Further increases of the shear rate, brings De close to 1, ignites the coarsening processes, and replaces the defect lattice with a defect gas. The topological charge of the defect gas is undetermined. The smallest texture length scale ℓ_t occurs at the defect lattice-defect gas transition. In the defect lattice regime the texture length scale ℓ_t decreases with increasing shear rate as $\ell_t \propto (\dot{\gamma} - a)^{-1/2}$, while in the defect gas regime it increases as $\ell_t \propto (\dot{\gamma} - b\sqrt{(\dot{\gamma} - a)} - c)^{-1}$. Finally when $De > 2$, a monodomain state emerges, and the texture vanishes since coarsening overpowers defect nucleation. It is found that the texture transition cascade unoriented monodomain$\Rightarrow$defect lattice$\Rightarrow$defect gas$\Rightarrow$oriented monodomain is remarkably consistent with the textural transition of sheared lyotropic tumbling nematic polymers.

ACKNOWLEDGMENTS

[1] A. D. Rey and M. M. Denn, Annu. Rev. Fluid Mech. **34**, 233 (2002).

[2] M. Kleman, Rep. Prog. Phys. **52**, 555 (1989).

[3] M. Kleman and Meyer, in *Defects in Liquid Crystals: Computer Simulations, Theory and Experiments* (Kluwer, Dordrecht, 2001), p. 201.

[4] R. G. Larson, *The Structure and Rheology of Complex Fluids* (Oxford University Press, New York, 1999).

[5] W. H. Han and A. D. Rey, J. Rheol. **39**, 301 (1995).

[6] F. Beekmans, A. D. Gotsis, and B. Norder, J. Rheol. **40**, 947 (1996).

[7] V. M. Ugaz, W. R. Burghardt, W. Zhou, and J. Kornfield, J. Rheol. **45**, 1029 (2001).

[8] P. G. De Gennes and J. Prost, *The Physics of Liquid Crystals*, 2nd ed. (Oxford University Press, London, 1993).

[9] A. D. Rey, Liq. Cryst. **7**, 315 (1990).

[10] A. D. Rey and M. M. Denn, Liq. Cryst. **4**, 409 (1990).

[11] A. D. Rey and T. Tsuji, Macromol. Theory Simul. **7**, 623 (1998).

[12] A. Sonnet, A. Kilian, and S. Hess, Phys. Rev. E **52**, 718 (1995).

[13] C. Denniston, E. Orlandini, and J. M. Yeomans, Europhys. Lett. **52**, 481 (2000).

[14] W. Helfrich, Phys. Rev. Lett. **21**, 1518 (1968).

[15] L. M. Blinov, *Electro-Optical and Magneto-Optical Properties of Liquid Crystals* (Wiley, New York, 1983).

[16] F. Lonberg, S. Fraden, A. J. Hurd, and R. B. Meyer, Phys. Rev. Lett. **52**, 1903 (1984).

[17] G. Srajer, S. Fraden, and R. B. Meyer, Phys. Rev. A **39**, 4828 (1989).

[18] M. Srinivasaro, in *Liquid Crystals in the Nineties and Beyond*, edited by S. Kumar (World Scientific, Singapore, 1995), p. 377.

[19] S. D. Hudson and E. L. Thomas, Phys. Rev. Lett. **62**, 1993 (1989).

[20] A. M. Donald and A. H. Windle, *Liquid Crystalline Polymers* (Cambridge University Press, Cambridge 1992).

[21] C. R. Fincher, Macromolecules **19**, 2431 (1986).

[22] R. B. Meyer, F. Lonberg, V. Taratuta, S. Fraden, S. D. Lee, and A. J. Hurd, Discuss. Chem. Soc. **79**, 125 (1985).

[23] A. J. Hurd, S. Fraden, F. Lonberg, and R. B. Meyer, J. Phys. (Paris) **46**, 905 (1985).

[24] L. Leger, Mol. Cryst. Liq. Cryst. **24**, 33 (1973).

[25] A. P. Singh and A. D. Rey, Rheol. Acta **37**, 374 (1998).

[26] P. T. Mather, D. S. Pearson, and R. G. Larson, Liq. Cryst. **20**, 527 (1996).

[27] P. T. Mather, D. S. Pearson, and R. G. Larson, Liq. Cryst. **20**, 539 (1996).

[28] D. J. Graziano and M. R. Mackley, Mol. Cryst. Liq. Cryst. **106**, 103 (1984).

[29] T. De'Neve, P. Navard, and M. Kleman, J. Rheol. **37**, 515 (1993).

[30] M. Srinivasaro and G. C. Berry, J. Rheol. **35**, 379 (1991).

[31] R. G. Larson and D. W. Mead, Liq. Cryst. **12**, 751 (1992).

[32] R. G. Larson and D. W. Mead, Liq. Cryst. **15**, 151 (1993).

[33] J. Vermant, P. Moldenaers, S. J. Picken, and J. Mewis, J. Non-Newtonian Fluid Mech. **53**, 1 (1994).

[34] Z. Tan and G. C. Berry, J. Rheol. **47**, 73 (2003).

[35] P. T. Mather, H. G. Jeon, C. D. Han, and S. Chang, Macromolecules **33**, 7594 (2000).

[36] W. R. Burghardt, Macromol. Chem. Phys. **199**, 471 (1998).

[37] F. Beekmans, A. D. Gotsis, and B. Norder, J. Rheol. **40**, 947 (1996).

[38] P. Manneville and E. Dubois-Violette, J. Phys. (Paris) **37**, 285 (1976).

[39] P. Manneville, J. Phys. (Paris) **39**, 911 (1978).

[40] E. Dubois-Violette and P. Manneville, in *Pattern Formation in Liquid Crystals*, edited by Agnes Buka and Lorenz Kramer (Springer, New York, 1995), p. 91.

[41] R. G. Larson, J. Rheol. **37**, 175 (1993).

[42] M. C. Calderer and B. Mukherjee, Physica D **98**, 201 (1996).

[43] W. H. Han and A. D. Rey, Phys. Rev. E **49**, 597 (1994).

[44] W. H. Han and A. D. Rey, Macromolecules **28**, 8401 (1995).

[45] G. Rienacker, M. Kroger, and S. Hess, Physica A **315**, 537 (2002).

[46] H. Pleiner and H. R. Brand, in *Pattern Formation in Liquid Crystals*, edited by A. Buka and L. Kramer (Springer-Verlag, Berlin, 1996), p. 15.

[47] H. Tu, G. Goldbeck-Wood, and A. H. Windle, in *Defects in Liquid Crystals: Computer Simulations, Theory and Experiments* (Ref. [3]), p. 201.

[48] M. G. Forest, Q. Wang, and H. Zhou, Phys. Rev. E **61**, 6655 (2000).

[49] G. Sgalari, G. L. Leal, and J. J. Feng, J. Non-Newtonian Fluid Mech. **102**, 361 (2002).

[50] T. Tsuji and A. D. Rey, J. Non-Newtonian Fluid Mech. **73**, 127 (1998).

[51] A. P. Singh and A. D. Rey, J. Non-Newtonian Fluid Mech. **94**, 87 (2000).

[52] F. M. Leslie, in *Advances in Liquid Crystals* (Academic Press, New York, 1979), p. 235.

[53] F. R. S. Chandrasekhar, *Liquid Crystals*, 2nd ed. (Cambridge, University Press, Cambridge, 1992).

[54] T. Carlsson, Mol. Cryst. Liq. Cryst. **89**, 57 (1982).

[55] F. M. Leslie, J. Phys. D **9**, 925 (1976).

[56] O. S. Tarasov, A. P. Krekhov, and L. Kramer, Liq. Cryst. **28**, 833 (2001).

[57] P. Pieranski and E. Guyon, Solid State Commun. **13**, 435 (1973).

[58] M. Remoissenet, *Waves Called Solitons—Concepts and Experiments* (Springer-Verlag, Berlin, 1999).

[59] G. Marrucci and F. Greco, in *Advances in Chemical Physics* (Wiley, New York, 1993), p. 331.